Technical University of Munich

Master's Thesis

Sensitivity Studies for the KATRIN Experiment

Author
Anna Magdalena Schubert

Supervisor
Prof. Dr. Susanne Mertens

February 9, 2023

Declaration of Authorship

I confirm that this Master's thesis is my own work and I have documented all sources and material used.

This thesis was not previously presented to another examination board and has not been published.

Anna Magdalena Schubert

Munich, February 9, 2023

Summary

The KArlsruhe TRItium Neutrino (KATRIN) experiment is designed to probe the neutrino mass down to $m_{\nu_\mathrm{e}} < 0.2\,\mathrm{eV/c^2}$ at 90 % C.L. using the kinematics of tritium beta decay. KATRIN started taking data in 2018, and published a leading limit on the neutrino mass of 0.8 eV in 2022. This Master's thesis investigates the expected final sensitivity and possible sensitivity improvements of the experiment. To this end, a neural-network-based analysis framework is used.

A realistic estimation of the sensitivity that can be reached by the end of 2025 (after 1000 days of data taking) is performed. It is found that, given the current operating parameters, a sensitivity of $m_{\nu_\mathrm{e}} < 0.3\,\mathrm{eV/c^2}$ at 90 % C.L. is achievable.

Further, various means to improve the sensitivity beyond this value, either within the 1000 days or beyond, are investigated. The study considers on the one hand the option of enhancing the statistics by means of increasing the data taking efficiency, enlarging the analysis window, and increasing the acceptance angle, and on the other hand the option of reducing the background. It could be shown that an enlarged analysis window is a very promising path, under the condition that certain systematic uncertainties are further reduced. The option of an enlarged acceptance angle brings a similar statistical improvement, however, would require too many substantial modifications of the experiment and is thus not a preferred solution. Various means to reduce the background are currently under investigation by the collaboration. The study in this thesis shows that these methods can be beneficial for the sensitivity and it provides a guidance of when they should be implemented to optimize the final KATRIN result.

Contents

Chapter 1

Introduction

Neutrinos are amongst the most abundant particles in the universe. They play a key role in various hot topics of modern day physics, such as the matter anti-matter asymmetry and structure formation in the early universe. In the standard model of particle physics neutrinos are predicted to be mass-less, but neutrino oscillation experiments could prove that they contrarily do have a non-zero mass. This mass is however extremely small, compared to other fermions and the underlying mass generation mechanism remains opaque.

The KArlsruhe TRItium Neutrino (KATRIN) experiment is designed to set an unprecedented limit on the electron anti-neutrino mass, examining the kinematics of the β-decay of molecular tritium. The goal sensitivity is $m_{\nu_e} < 0.2\,\mathrm{eV/c^2}$ at 90 % C.L. after five years of data taking. This thesis was performed to study the feasibility of that objective and investigate possible ways to optimize the final KATRIN sensitivity. This was done by performing various sensitivity studies, considering current, previous and hypothetical future scenarios. The thesis is structured in the following way:

In chapter 2, an introduction to neutrino physics is given. Their role in the standard model of particle physics is explained, as well as neutrino flavor oscillations. Further, the three approaches to access the absolute neutrino mass scale are introduced: Cosmology, the neutrino-less double β-decay, as well as β-decay kinematics.

The KATRIN experiment is then described in chapter 3. The first part focuses on the experimental set-up, the second part explains the model of the tritium β-decay spectrum and at the end, sources of systematic uncertainties are introduced.

In chapter 4, the methodology of sensitivity studies in KATRIN is described. As a foundation, the whole neutrino mass analysis procedure is explained. Then the concepts of sensitivity and discovery potential are introduced and finally the validation for the sensitivity and discovery potential calculation approach is presented.

Chapter 5 covers all sensitivity scenarios that have been investigated in the course of this thesis. Incipiently, the assumptions that underlie the subsequent scenarios are explained. The first group of investigated scenarios then covers the current and a previous measurement set-up. Secondly, two scenarios are examined that would yield a signal enhancement: A fit range extension as well as an acceptance angle enlargement. Furthermore, two scenarios with a reduced background rate are presented: The current setting with the originally designed background rate as well as the impact of a novel active transversal energy filter that could reduce the background by a factor of three.

For all investigated scenarios a sensitivity prospect is given. At the end, a conclusive prospect is given for the final KATRIN sensitivity as well as for the 3σ and 5σ discovery potential.

Chapter 2

Neutrino physics

Neutrinos carry plenty of information about various open topics in physics. The following chapter provides an introduction to the history of neutrinos as well as to their physical properties. A short overview of neutrino oscillations is given. To further understand the purpose and the functionality of the KATRIN experiment, different observables of the neutrino masses are introduced.

2.1 Discovery of the neutrino

The neutrino was first postulated in 1930 by Wolfgang Pauli to explain the continuity of the β-decay electron spectrum [1]. The energy signal was expected to be peak-like as the electron would receive besides the recoil energy the total released energy of the decay and the energy of the daughter nucleus is known and constant. Instead, a continuous spectrum was observed which could be explained as a three-body decay by adding a neutrally charged spin-$\frac{1}{2}$ particle the electron had to share the released energy with. Figure 2.1 shows both spectra in an explanatory way.

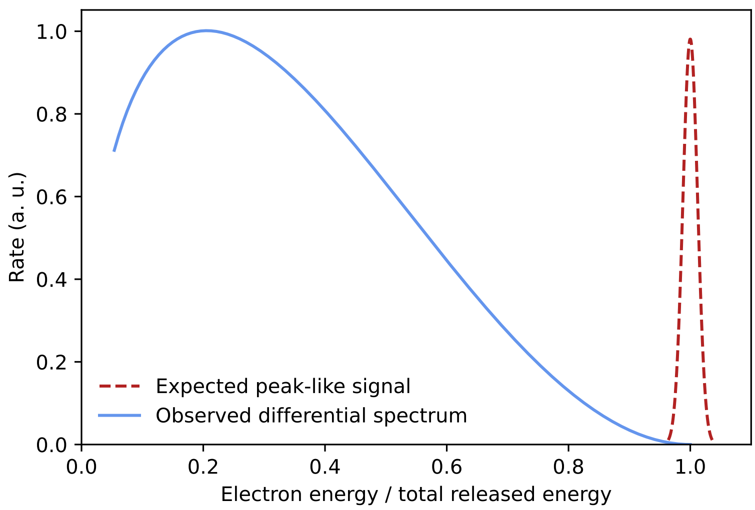

Figure 2.1: Electron energy spectrum of the β-decay. The dashed red line shows the expected peak-like signal: All β-electrons have the same energy. The blue line shows the experimentally observed continuous spectrum, which is only explainable under the consideration of an additional neutrino that receives a part of the energy.

In 1934 Enrico Fermi presented his theory of the β-decay and first named the postulated particle *neutrino* [2]. The β-decay of the neutron is e.g. in [3] expressed as

$$n \rightarrow p^+ + e^- + \overline{\nu}_e. \tag{2.1}$$

The experimental evidence for the neutrino followed in 1956 by Clyde L. Cowan and Frederick Reines. The experiment used the neutrino flux from Savannah River Plant of the V.S. Atomic Energy Commission. The incoming electron anti-neutrinos reacted with protons in water:

$$\overline{\nu}_e + p^+ \rightarrow e^+ + n \tag{2.2}$$

A multiple-layer arrangement of scintillation counters and target tanks was then used to detect the neutrino induced double-pulse signal: The first pulse due to the deceleration and annihilation of the positron and the second pulse due to neutron capture in cadmium [4].

2.2 Neutrinos in the standard model of particle physics

Neutrinos are spin-$\frac{1}{2}$ particles and hence fermions. They are uncharged leptons who underlie the weak interaction e.g. via the β-decay. They further underlie the gravitational interaction as they are now known to be massive. There are at least three different neutrinos which build each with their related negatively charged lepton (electron, muon, tauon) a lepton family:

$$\begin{pmatrix} \nu_e \\ e^- \end{pmatrix} \begin{pmatrix} \nu_\mu \\ \mu^- \end{pmatrix} \begin{pmatrix} \nu_\tau \\ \tau^- \end{pmatrix}$$

The distinction between the three lepton families (electron, muon, tauon) is called $flavor$. To each of these three families exists the corresponding family of anti-particles. The charged leptons have a significantly higher mass than their correspondingly flavored neutrinos. In the standard model of particles physics neutrinos are even proposed to be massless [5].

2.3 Neutrino oscillations

The assumption of the standard model of particle physics that neutrinos are massless was however disproved by the observation of neutrino oscillations, discussed in the following.

The three neutrino mass states $|\nu_1\rangle$, $|\nu_2\rangle$ and $|\nu_3\rangle$ each have a defined yet unknown mass but are not identical to the three neutrino flavor states $|\nu_e\rangle$, $|\nu_\mu\rangle$ and $|\nu_\tau\rangle$. Instead a neutrino of a defined flavor can be understood as a quantum mechanical linear combination of the three mass states and vice versa:

$$\begin{pmatrix} |\nu_e\rangle \\ |\nu_\mu\rangle \\ |\nu_\tau\rangle \end{pmatrix} = \begin{pmatrix} U_{e1} & U_{e2} & U_{e3} \\ U_{\mu 1} & U_{\mu 2} & U_{\mu 3} \\ U_{\tau 1} & U_{\tau 2} & U_{\tau 3} \end{pmatrix} \cdot \begin{pmatrix} |\nu_1\rangle \\ |\nu_2\rangle \\ |\nu_3\rangle \end{pmatrix} \tag{2.3}$$

The matrix $\mathbf{U}$ is called PMNS-matrix, named after Pontecorvo, Maki, Nakagawa and Sakata who all investigated neutrino mixing and oscillations of some kind. It is unitary and consists of three mixing angles and one phase.

For the simplified case of two neutrinos 2.3 reduces to

$$\begin{pmatrix} |\nu_\alpha\rangle \\ |\nu_\beta\rangle \end{pmatrix} = \begin{pmatrix} \cos(\theta) & \sin(\theta) \\ -\sin(\theta) & \cos(\theta) \end{pmatrix} \cdot \begin{pmatrix} |\nu_{\mathrm{I}}\rangle \\ |\nu_{\mathrm{II}}\rangle \end{pmatrix} \tag{2.4}$$

with mixing angle θ. Neutrinos are produced by weak interactions in a certain flavor state and propagate in their mass state which can be described by a wave function:

$$|\nu_\alpha(t)\rangle = \cos(\theta) e^{-iE_{\nu_{\mathrm{I}}}t/\hbar}|\nu_{\mathrm{I}}\rangle + \sin(\theta) e^{-iE_{\nu_{\mathrm{II}}}t/\hbar}|\nu_{\mathrm{II}}\rangle \tag{2.5}$$

The oscillation probability, and thus the probability to detect the neutrino in a different flavor state after a time t, is non-zero for a non-vanishing difference Δm^2 of the mass states $|\nu_{\mathrm{I}}\rangle$ and $|\nu_{\mathrm{II}}\rangle$ and can be expressed as

$$P_{\nu_\alpha \rightarrow \nu_\beta} = \sin^2(2\theta) \sin^2 \left(\frac{1}{4} \frac{\Delta m^2 c^4}{\hbar c} \frac{L}{pc} \right) \tag{2.6}$$

with L the so called oscillation length, the distance between two oscillation maxima. The observable of neutrino oscillations is the difference of the squared masses $\Delta m_{ij}^2 = m_i^2 - m_j^2$ and not the absolute neutrino mass. For more detail cf. [5].

The first experiments indicating neutrino oscillations were performed with solar neutrinos. The flux of electron neutrinos was by a factor two to three smaller than solar models predicted. The interpretation of that phenomenon were oscillations of the electron neutrinos into muon and tauon neutrinos [5]. The evidence for this assumption followed in 2002 by the SNO collaboration [6]. The first evidence for neutrino oscillations and hence non-zero neutrino masses was presented in 1998 in Takayama by the Super-Kamiokande collaboration [7, 8].

2.4 Determination of the absolute neutrino masses

As neutrino oscillation experiments can only investigate the difference of the squared mass states Δm_{ij}^2, different approaches are necessary to access the absolute neutrino mass scale. The three accessible approaches are presented in the following.

2.4.1 Cosmology

The value that cosmology has access to is the sum of all three neutrino masses $\sum m_\nu$ because it is related to the neutrino energy density Ω_ν which can be investigated. Massive neutrinos have an impact especially on two cosmological observables:

The Cosmic Microwave Background (CMB) temperature anisotropy power spectrum on the one hand is affected by the neutrino mass only through a modified background behaviour and certain anisotropy corrections.
The matter power spectrum by which large scale structures of the universe can be probed on the other hand is affected by the free streaming, caused by small neutrino masses $\mathcal{O}(\mathrm{eV})$ and hence the main observable in cosmology to set bounds on $\sum m_\nu$.
The observables are explained in great detail in [9].
The Planck collaboration currently sets upper limits for $\sum m_\nu$ with 95% Confidence Level (C.L.) between 0.12 eV and 0.60 eV, highly depending on the used model [10].

2.4.2 Neutrinoless double beta-decay

If neutrinos are Majorana particles, meaning they are their own anti particles, neutrinoless double β-decay (0νββ) could be observed. In 0νββ two neutrons decay into two protons and two electrons:

$$A \rightarrow B^{2+} + 2e^{-} \tag{2.7}$$

While in the regular neutrino accompanied double β-decay (2νββ) in addition to the two electrons in 2.7 two electron anti-neutrinos are emitted. In 0νββ the two neutrinos vanish as they behave as particle and anti-particle. The two electrons then share the entire released energy of the decay. The signature of the 0νββ would therefore be a peak like signal next to the 2νββ energy spectrum [11].

The value 0νββ experiments have access to is the effective Majorana neutrino mass

$$\langle m_{\beta\beta} \rangle = \Big| \sum_k U_{ei}^2 m_i \Big| \tag{2.8}$$

which is related to the lifetime of the 0νββ. The Majorana mass term 2.8 contains the three neutrino masses m_i and the mixing element U_{ei} which itself contains an unknown CP-violating Majorana phase. This phase could enable cancellations and therefore $\langle m_{\beta\beta} \rangle$ could be smaller than the individual m_i [12].

The 0νββ has not yet been observed but upper limits on the Majorana mass were set e.g. by the GERDA collaboration to $\langle m_{\beta\beta} \rangle < 0.079$ - $0.180\,\mathrm{eV}$ with 90% C.L. [11].

2.4.3 Electron β-decay spectrum

As seen in 2.1, in the three-body β-decay a neutron decays into a proton under emission of an electron and an electron anti-neutrino. The total released energy Q is shared between the recoiled daughter nucleus (E_{rec}), the electron (E) and the electron anti neutrino (E_ν). The so called endpoint energy

$$E_0 = E + E_\nu = Q - E_{\mathrm{rec}} \tag{2.9}$$

is the maximum energy the electron could carry away if the neutrino was massless.
The observable of the β-decay kinematics is the squared neutrino mass which is described by the incoherent sum of the neutrino masses:

$$m_{\nu_e}^2 = \sum_i \left|U_{ei}^2\right|^2 m_i^2. \tag{2.10}$$

Using Fermi's golden rule the observed differential β-decay rate depending on the electron energy can be expressed as

$$\frac{\mathrm{d}\Gamma}{\mathrm{d}E} = \frac{G_{\mathrm{F}}^2 \cos^2(\theta_{\mathrm{C}})}{2\pi^3} \cdot |M_{\mathrm{nuc}}|^2 \cdot F(Z,E) \cdot p(E+m_e) \cdot E_\nu \sqrt{E_\nu^2 - m_\nu^2} \cdot \Theta(E_\nu - m_\nu) \tag{2.11}$$

with the Fermi coupling constant G_F, the Cabbibo angle θ_C, the nuclear transition matrix element M_{nuc} and the momentum of the outgoing electron p. The classical Fermi function $F(Z,E)$ accounts for Coulomb interaction between the electron and the daughter nucleus. The Heaviside function Θ only allows positive kinetic energies and thus ensures energy conservation [13].

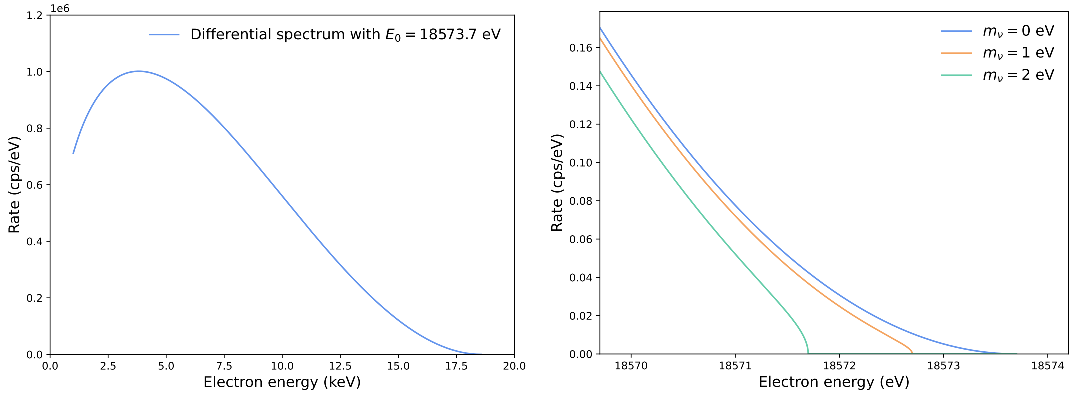

(a) Differential electron energy spectrum of the β-decay in full energy range.

(b) Differential spectrum with different Neutrino masses in endpoint region.

Figure 2.2: Differential electron energy spectrum of the β-decay. In the endpoint region the impact of different neutrino masses can be seen. For higher neutrino masses the maximum electron energy is shifted to lower energies.

The differential electron energy spectrum of the β-decay is shown in figure 2.2. On the left the full energy range is displayed while the figure on the right shows the spectrum in the endpoint region, considering different neutrino masses. For higher neutrino masses the maximum electron energy is lowered. In this region also the shape distortion due to non-zero neutrino masses is observable. Mostly because of very low statistics in the endpoint region and the overall background, it is usually not feasible to resolve the lowered maximum energy. Therefore the main observable of experiments which investigate the neutrino mass via β-decay kinematics is the above seen shape distortion of the spectrum.

The KArlsruhe TRItium Neutrino (KATRIN) experiment currently can set the tightest constraints on the neutrino mass. It is located in Karlsruhe, Germany and investigates the neutrino mass via tritium β-decay. The goal sensitivity of KATRIN is 0.2 eV at 90% C.L. and the current published upper limit KATRIN can set on m_ν is 0.8 eV [14]. The KATRIN experiment is introduced in more detail in the following chapter.

Chapter 3

The KATRIN experiment

The KArlsruhe TRItium Neutrino (KATRIN) experiment is located at Karlsruhe Institute of Technology (KIT) in Germany, exploiting resources of the Tritium Laboratory Karlsruhe (TLK). It started taking data in 2018 and aims to constrain the neutrino mass from β-decay kinematics to 200 meV. It follows the principle of two previous similar experiments: The Mainz experiment with a final upper limit on the neutrino mass of 2.3 eV [15] and the Troitsk nu-mass experiment with a final upper limit on m_ν of 2.2 eV [16]. As explained in 2.4.3 the observable of experiments investigating β-decay kinematics is the effective mass of the electron anti-neutrino

$$m_{\nu_e} = \sqrt{\sum_i \left|U_{ei}^2\right|^2 m_i^2}. \tag{3.1}$$

This chapter introduces the experimental set-up of the KATRIN experiment as well as the model of the beta-decay spectrum. Further, sources of systematic uncertainties are explained. For a more detailed overview cf. [17] (set-up) and [13] (modelling).

3.1 Experimental set-up

The KATRIN experiment is built as a complex apparatus of 70 m length. The main parts are the following. They are shown in figure 3.1 and will be described in this chapter.

a **Rear section** containing the electron gun (e-gun) for calibration purposes and the rear wall (RW) to control plasma properties.

b **Windowless Gaseous Tritium Source (WGTS)** to provide pure tritium gas with stable density.

c **Transport system** containing the Differential Pumping System (DPS) and the Cryogenic Pumping System (CPS) to guide the electrons towards the spectrometer and to prevent the tritium from entering it.

d **Pre-spectrometer** to reject all electrons with energies less than 300 eV below the endpoint.

e **Main spectrometer** to filter electrons by their energy using a MAC-E filter.

f **Detector section** with 148-pixel Focal Plane Detector (FPD) and data acquisition (DAQ) system.

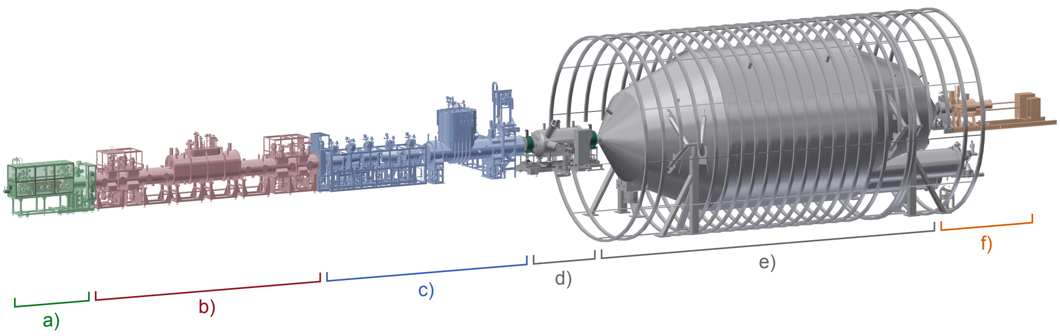

Figure 3.1: Beamline of the 70 m long KATRIN experiment: a) Rear section. b) Windowless Gaseous Tritium Source (WGTS). c) Transport system. d) Pre-spectrometer. e) Main spectrometer. f) Segmented Focal Plane Detector (FPD). Figure provided by Leonard Köllenberger.

3.1.1 Rear section for monitoring and calibration

The rear section contains the rear wall (RW) of the WGTS. It is a stainless steel disk coated with gold with a 14.5 cm diameter. By adjusting the RW surface potential the plasma potential distribution can be controlled.

Other than that a high resolution angular selective electron gun (e-gun) is mounted in the rear section of the KATRIN experiment. It emits a pulsed electron beam with well known rate R_g, angle Θ and energy E with a spread of $< 0.5\,\mathrm{eV}$ which can be held stable over several hours. The e-gun is especially used for calibrations as it allows investigations of electromagnetic properties along the beam line and source characteristics, such as scattering and hence energy loss effects as well as the column density stability.

3.1.2 Windowless gaseous tritium sorce

The ultra-luminous Windowless Gaseous Tritium Source (WGTS) of the KATRIN experiment uses a 10 m long beam tube with 9 cm diameter. The tube is continuously filled with molecular gaseous tritium. It can provide an activity up to 10^{11} Bq as the tritium decays via the β-decay. Using magnetic fields, the β-electrons are then guided towards the spectrometer. The nominal setting of the magnetic fields allows electrons with a starting angle up to 51° w.r.t. the magnetic field to be transmitted. To avoid energy loss effects of the electrons (except inelastic scattering inside the gas) the tube is windowless. At the ends of the tube the tritium molecules are pumped away in order to avoid a contamination of the spectrometer. A cryostat system allows low conductance of the tube and hence a constant reference column density of 5.0×10^{17} molecules/cm^2. Pump ports and a tritium loop system in the WGTS magnet-cryostat prevent a tritium flow into the spectrometer.

3.1.3 Transport section

The transport section consists of the Differential Pumping System (DPS) and the Cryogenic Pumping System (CPS). The purposes are to adiabatically guide the β-electrons from the WGTS to the spectrometer and to reduce the tritium flow into the spectrometer by 12 orders of magnitude. As this system is S-shaped the charged electrons are magnetically guided through the system while uncharged molecules get deflected and pumped away.

The DPS is located between the WGTS and the CPS. The adiabatic electron guiding is realised by five superconducting magnets, each with a maximum magnetic field of 5 T. The magnets are cooled with liquid helium. The tritium flow into the spectrometer is reduced by differential pumping.

The CPS is located right before the spectrometer section and contains another superconducting magnet. Here tritium molecules get adsorbed by an argon frost layer on the tube surface. It offers high pumping speed and long term tritium retention during operation. In stand-by mode the removal of tritium from the beam tube surface is easy.

3.1.4 Spectrometer section with MAC-E filter

The spectrometer section consists of a pre-spectrometer and a main spectrometer. The pre-spectrometer is designed to reject all electrons with an energy less than 18.3 keV to reduce background. This has no impact on the spectrum distortion as these electrons have an energy too far from the endpoint. As it showed however, at the ends of the pre-spectrometer so called penning traps form, which instead increase the background. Hence, the pre-spectrometer is no longer in use.

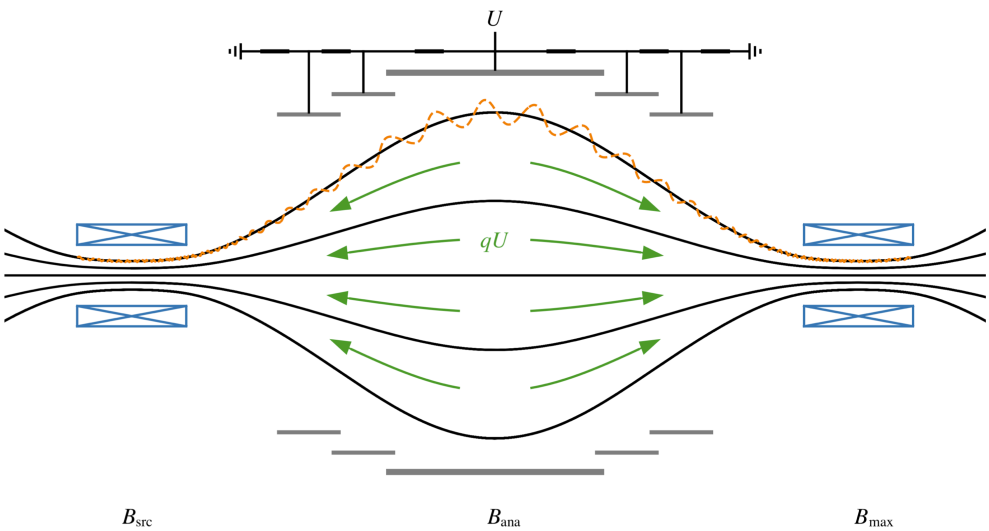

Figure 3.2: Schematic overview of the MAC-E filter. The electron energy becomes mostly transversal along the magnetic field gradient between B_{source} and B_{ana}. Energy and magnetic moment of the cyclotron motion (orange dashed line) are conserved. In the analyzing plane (lowest magnetic field) electrons with insufficient energy, defined by the applied retarding potential U, are rejected. The transmitted electrons are re-accelereted towards the detector by an again increasing magnetic field up to B_{max}. Figure taken from [18].

For the spectroscopy in the KATRIN experiment a Magnetic Adiabatic Collimation with Electrostatic (MAC-E) filter is used in the pre-spectrometer as well as in the main spectrometer. The MAC-E filter is illustrated in figure 3.2. In the source electrons are emitted isotropically. They are then guided adiabatically by magnetic fields towards the spectrometer. Along their path the electrons have a longitudinal energy component $E_\perp$ and a transversal energy component $E_\parallel$ and they perform cyclotron motion with magnetic moment μ and angular momentum $\vec{l}$ around the magnetic field lines. At both ends of the spectrometer high magnetic fields B_{source} and B_{max} are applied. In forward direction the magnetic field in the spectrometer decreases by several orders of magnitude down to a minimum magnetic field B_{ana} $\mathcal{O}(0.5\,\mathrm{mT})$. This field gradient yields an adiabatic transformation of $E_\perp$ to $E_\parallel$ under conservation of μ and $\vec{l}$:

$$\mu = \frac{e}{2m_{\mathrm{e}}}|\vec{l}| = \frac{E_\perp}{B} = const. \tag{3.2}$$

A negative voltage is applied to the spectrometer vessel, creating the so called retarding potential U which is largest at the point of the lowest magnetic field. This point defines the so called analyzing plane as only electrons with transversal energy $E_\parallel > eU$ can pass this plane. Here the MAC-E filter acts as an electrostatic high-pass filter. As the magnetic field then increases again up to B_{max}, the transmitted electrons are re-accelerated towards the detector. The reflected electrons are re-accelerated towards the entrance of the spectrometer.
The energy resolution, also called filter width of the MAC-E filter is constrained by the remaining transversal energy component of the electron at the analyzing plane and is given by

$$\Delta E = \frac{B_{\mathrm{ana}}}{B_{\mathrm{max}}} \cdot E\frac{\gamma+1}{2} \tag{3.3}$$

with the kinetic energy of the electron E and the relativistic gamma factor $\gamma = \frac{E+m_{\mathrm{e}}}{m_{\mathrm{e}}}$ with the electron rest mass m_{e}. The maximum acceptance angle w.r.t. the magnetic field lines in which electrons can still reach the detector is

$$\Theta_{\mathrm{max}} = \arcsin\left(\sqrt{\frac{B_{\mathrm{source}}}{B_{\mathrm{max}}}}\right). \tag{3.4}$$

In the nominal KATRIN setting the maximum acceptance angle is set to $\Theta_{\mathrm{max}} = 51°$.

3.1.5 Detector section

The β-electrons selected by the KATRIN main spectrometer are detected by the multi-pixel Focal Plane Detector (FPD). The electrons are adiabatically guided towards the detector by two superconducting magnets. In the nominal KATRIN setting a flux tube of $134\,\mathrm{Tcm}^2$ then arrives at the FPD. To reduce the backscattering probability and shift the signal into a lower background region the electrons are accelerated before they arrive at the detector. A main challenge is to operate the FPD system at very low pressure as it is coupled to the main spectrometer.

The FPD itself is a 148-pixel *p-i-n* diode array mounted on a 503 µm silicon wafer with 12.5 cm diameter. Each pixel has a diameter of $44\,\mathrm{mm}^2$. Due to noise, some misalignment and other pixel characteristics usually not all pixels are used in the neutrino mass analysis. The DAQ system makes use of up to nearly 500 channels which are necessary to cover the whole needed range from single-channel rates of 1-1000 cps up to an above 1 Mcps rate over the whole detector.

3.2 Model of the β-decay spectrum

To obtain the full model of the β-decay of molecular tritium in KATRIN, several effects have to be taken into account which is why additional corrections to the decay rate have to be made, as explained in the following.

3.2.1 Final state distribution

In chapter 2.4.3 the differential decay rate of atomic tritium was introduced as equation 2.9. As however the β-decay of molecular tritium

$$\mathrm{T}_2 \rightarrow^3 \mathrm{HeT}^+ + e^- + \bar{\nu}_e \tag{3.5}$$

is considered, some additional corrections have to be made. As the tritium molecule decays, the recoil shifts the daughter molecule into a certain final state f with an energy V_f. The final state can be rotational, vibrational or electrically excited. Considering this correction the neutrino energy is then

$$E_\nu \rightarrow E_{\nu,f} = E_0 - V_f - E. \tag{3.6}$$

In the differential decay rate the summation over all final states f with energy V_f weighted by their probability p_f has to be considered:

$$\frac{\mathrm{d}\Gamma}{\mathrm{d}E} = \frac{G_\mathrm{F}^2 \cos^2(\theta_\mathrm{C})}{2\pi^3} \cdot |M_\mathrm{nuc}|^2 \cdot F(Z,E) \cdot p(E+m_\mathrm{e}) \cdot \sum_f p_f E_{\nu,f} \sqrt{E_{\nu,f}^2 - m_\nu^2} \cdot \Theta(E_{\nu,f} - m_\nu) \tag{3.7}$$

Theoretical calculations of the Final State Distribution (FSD) find that about 57% of the T_2 decays leave the daughter molecule in either a rotational or vibrational ground state with an average excitation energy of 1.7 eV while the others proceed into excited electronic states [19].

3.2.2 Doppler effect

As the tritium molecules perform thermal motion in the source, the differential spectrum gets broadened due to the Doppler effect. The Doppler broadening has a value of

$$\sigma_D = \sqrt{2E \cdot k_\mathrm{B} T \cdot \frac{m_\mathrm{e}}{M_{\mathrm{T}_2}}} \tag{3.8}$$

with the electron energy E, the Boltzmann constant k_B, the source temperature T and the electron mass m_e as well as the mass of the tritium molecules M_{T_2}. This effect is only considered in the neutrino mass analysis as a smearing of the FSD.

3.2.3 Response function

The so called response function covers two individual effects: The transmission of the MAC-E filter and energy losses of electrons travelling through the source. In the ideal case the transmission at the MAC-E filter would be described by a step function at $E = qU$, as all electrons with sufficient energy would pass the analyzing plane and all others be stopped and accelerated backwards. As introduced in 3.1.4, the MAC-E filter however has a certain filter width ΔE as the electrons can have a residual transversal energy component. If an electron can pass the analyzing plane, and hence the filter, depends on its energy E and its starting angle θ. The electron can only pass the filter if the following condition for θ is fulfilled:

$$\cos(\theta) > \sqrt{1 - \frac{E - qU}{E} \frac{B_{\text{source}}}{B_{\text{ana}}} \frac{2}{\gamma + 1}} \tag{3.9}$$

A full derivation for this condition is provided in [18]. This results in the transmission function

$$\mathcal{T}(E, qU) = \begin{cases} 0, & \varepsilon < 0 \\ 1 - \sqrt{1 - \frac{\varepsilon}{E} \frac{B_{\text{source}}}{B_{\text{ana}}} \frac{2}{\gamma+1}}, & 0 < \varepsilon < \Delta E \\ 1 - \sqrt{1 - \frac{B_{\text{source}}}{B_{\text{max}}}}, & \varepsilon > \Delta E \end{cases} \tag{3.10}$$

with the so called surplus energy $\varepsilon = E - qU$, again the relativistic gamma factor $\gamma = \frac{E + m_{\text{e}}}{m_{\text{e}}}$ and the filter width ΔE from equation 3.3. The transmission function has to be slightly corrected for synchrotron radiation losses the electrons experience while travelling along the beam-line.

As the electrons travel through the gaseous source they happen to scatter inelastically with tritium molecules along their way. There are two properties to take into account when quantizing energy loss due to scattering: First, the energy loss function $f(\epsilon)$ which describes the probability that a scattering causes a loss of energy ϵ. And second, the scattering probability functions $P_s(\Theta)$ for electrons with starting angle Θ to scatter s times inside the source.

Inelastic scattering in the source causes electronic excitations and rotational and vibrational excitations of the molecule, ionization, and molecular dissociation. The energy loss function $f(\epsilon)$ contains a parametrisation with three Gaussians, each of which approximates one group of final states. Ionisation effects with higher energies are covered by the relativistic Binary Encounter Dipole (BED) model. The full energy loss function is hence

$$f(\epsilon) = \begin{cases} \sum_{j=1}^{3} a_j \cdot \exp\left(-\frac{(\epsilon - m_j)^2}{2\sigma_j^2}\right), & \epsilon \leq \epsilon_i \\ \frac{f(\epsilon_i)}{f_{\text{BED}}(\epsilon_i)} \cdot f_{\text{BED}}(\epsilon), & \epsilon > \epsilon_i \end{cases} \tag{3.11}$$

with energy loss ϵ, ionisation threshold ϵ_i, and a_i, m_i and σ_i the amplitude, mean and width of the three Gaussians. f_{BED} is the functional form of the BED model. For more detail cf. [20].

Depending on the column density ρd, the probabilities P_s for electrons travelling through the source to scatter s times can be calculated. P_s further depend on the electron's position z in the source and the starting angle Θ, as increasing these leads to an increased path through the source. This results in a higher scattering probability and can later be taken into account as a larger effective column density. The mean scattering probabilities $\overline{P}_s$ are obtained by integrating over the length L and density profile $\rho(z)$ of the source:

$$\overline{P}_s = \frac{1}{\rho d} \int\limits_{z=-L/2}^{+L/2} \rho(z) \cdot \overline{P}_s(z) \mathrm{d}z \tag{3.12}$$

For a constant magnetic field over the source the scattering probabilities are independent of $\rho(z)$. Combining the transmission function and the scattering effects, the response function is obtained for s up to N scatterings with probabilities P_s and energy loss functions $f_s(\epsilon)$:

$$\mathcal{R}(E, qU) = \int_{\epsilon=0}^{E-qU} \sum_{s=0}^{N} \mathcal{T}(E-\epsilon, qU) \cdot \overline{P}_s \cdot f_s(\epsilon) \mathrm{d}\epsilon \tag{3.13}$$

For $s = 0$ (electron did not scatter in the source and hence did not lose energy) $f_0(\epsilon) = \delta(\epsilon)$. For s scatterings $f(\epsilon)$ is convoluted s times [21]. An example for the response function in the ideal case, the case of considering a filter width but no column density and the here derived full case, including filter width and scatterings, is shown in figure 3.3.

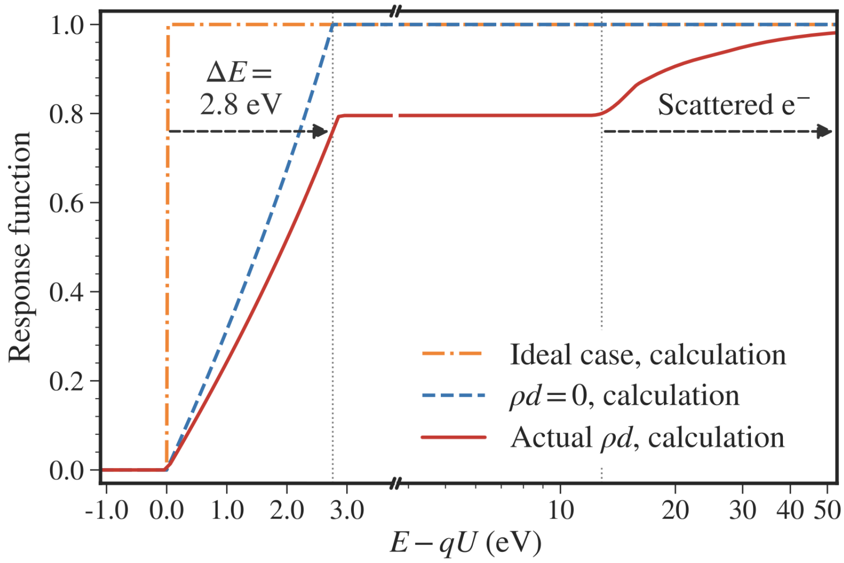

Figure 3.3: The Response function is in the ideal case described by a step function (orange). Considering the filter width it gets less sharp (blue). Scattering effects have an additional characteristic imprint (red). Electrons need additional surplus energy to overcome the potential barrier. For higher energy electrons the transmission is also possible after energy loss due to source scattering. At 18.6 keV the filter width of the KATRIN experiment is $\Delta E = 2.8$ eV. Figure taken from [22].

3.2.4 Integral spectrum

The MAC-E filter acts as an integral filter as for every investigated retarding potential all electrons with the threshold energy or higher can pass. KATRIN therefore actually measures the integrated β-spectrum. The model of the integral spectrum is obtained by integrating over the theoretical prediction of the differential tritium β-spectrum $\frac{\mathrm{d}\Gamma}{\mathrm{d}E}(E)$ and the experimental response function $\mathcal{R}(E, qU)$. A normalization factor $\mathcal{A}$ carries information about the signal strength. Background phenomena are denoted in $\mathcal{B}$. The expected electron rate is then

$$\mathcal{I}(qU) = \mathcal{A} \cdot \int_{qU}^{\infty} \frac{\mathrm{d}\Gamma}{\mathrm{d}E}(E) \cdot \mathcal{R}(E, qU) \mathrm{d}E + \mathcal{B} \tag{3.14}$$

The normalization factor $\mathcal{A}$ contains the effective number of tritium atoms, the acceptance angle and hence information about the magnetic fields and the efficiency of the detector.

To convert the rate $\mathcal{I}(qU)$ into the expected number of counts it is multiplied by the measurement time at each retarding potential qU [23]:

$$\mu(qU) = \mathcal{I}(qU) \cdot t(qU) \tag{3.15}$$

The Measurement Time Distribution (MTD) is optimized in a way that the neutrino mass imprint is maximal. A typical countrate at the detector is shown in an explanatory way in figure 3.4 considering up to 4 scatterings.

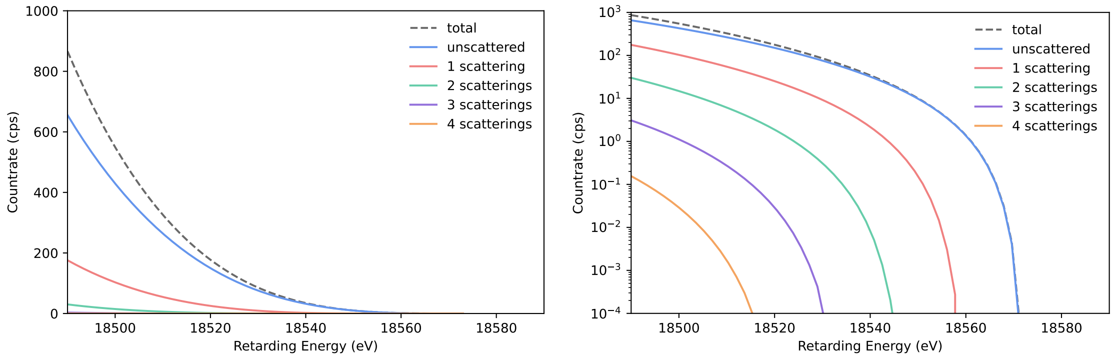

(a) Electron energy spectrum in endpoint region depending on number of scatterings.

(b) Electron energy spectrum in endpoint region depending on number of scatterings, log-scale.

Figure 3.4: Amount of zero to four times scattered electrons at the detector in a typical integrated electron energy spectrum. The spectrum is dominated by unscattered electrons. For better visibility of higher scatterings a log-scale is used (b).

3.3 Systematic uncertainties

Systematic uncertainties are due to uncertainties of parameters that influence the model calculation and due to instabilities of experimental parameters. To perform a robust analysis it is necessary to reliably consider the uncertainties of the various systematic effects. Otherwise the neutrino mass result can be biased [22]. The individual systematic effects are explained in the following. As in this work different hypothetical and real experimental settings are investigated, actual values for systematic parameters and their uncertainties are only given in the corresponding chapters later in the thesis.

Column density As seen above, electrons scatter with tritium molecules in the source. This effect is quantified by $\rho d\sigma_{\text{inel}}$, the product of the column density ρd and the inelastic scattering cross section $\sigma_{\text{inel}} = 3.637 \times 10^{-22}\,\text{m}^{-2}$. The column density can only be determined up to some uncertainty. This uncertainty propagates into the response function (equation 3.13), and hence into the model of the integral spectrum (equation 3.14). The column density is determined using the electron gun introduced in 3.1.1. It emits a high rate of 18.6 keV monoenergetic electrons. The electron rate at the detector is measured for different retarding potentials and then fitted to the model response function in a two parameter fit, including the electron rate and $\rho d\sigma_{\text{inel}}$. In this way the $\rho d\sigma_{\text{inel}}$ and its uncertainty can be determined. A throughput sensor in the transport section further allows a determination of the column density also during regular tritium scans. This information is combined with the e-gun results [24].

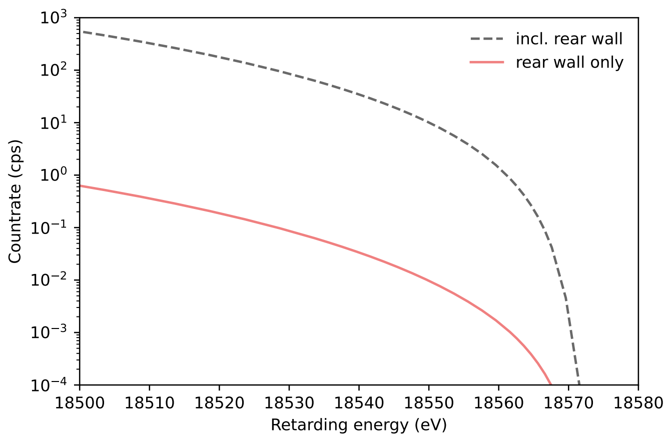

Figure 3.5: Example for a regular KATRIN spectrum including the RW spectrum (black dashed line) and the corresponding RW spectrum only (red line).

Rear wall The rear wall as introduced in 3.1.1, is a steel disc in the rear part of the KATRIN experiment, located before the WGTS. Tritium molecules from the source can accumulate on the RW and decay later. This effect is modelled as an additional β-spectrum. The uncertainties due to this additional spectrum arise from the uncertainty on the endpoint of the RW spectrum $E_{0,\text{RW}}$ and on the amount, and hence the activity, of the residual tritium on the RW. The amount of residual tritium increases over time as it depends on the integrated flux of circulated tritium gas. The RW can be cleaned between measurement phases using ozone [25]. An example for a RW spectrum is given in figure 3.5.

Energy loss function The energy loss function (eq. 3.11) can be investigated as it enters the response function (eq. 3.13). All parameters of the energy loss function as well as their uncertainties are determined by fitting the parameters to measurements of the response function, taken with the e-gun. This results in a 9×9 covariance matrix K_{eloss} which is considered when fitting neutrino mass data. The uncertainty on the energy loss function propagates into an uncertainty on the response function [20].

Magnetic fields The transmission function (eq. 3.10) directly depends on the ratio of the source magnetic field B_{source} and the pinch magnetic field B_{max} to the magnetic field in the analyzing plane B_{ana}. Their location is visualized in figure 3.2. B_{max} directly influences the transmission function as is defines the filter width of the MAC-E filter (cf. eq. 3.3). The impact of B_{source} is smaller.
Other than that B_{source} and B_{max} define the acceptance angle (cf. eq. 3.4). A change in the acceptance angle translates into a de- or increased signal amplitude. This is taken into account via the signal normalization, which does not impact the neutrino mass analysis. The scattering probabilities however, are also dependent on angular adjustments in terms of changes in the shape of the response function. Therefore, the different scattering probabilities have to be considered when propagating uncertainties [18].

Source plasma The potential in the source and its uncertainty effect the tritium β-spectrum. Variations of this spatially and time dependent potential lead to shape distortions of the spectrum. The source potential emerges from a low density plasma in the source. Plasma describes the occurrence of free charge carriers in the source volume. These are the β-electrons and $^3\text{HeT}^+$ ions produced in the tritium decay with a rate of $\sim 10^{11}$ per second and $\mathcal{O}(50)$ times more secondary electrons from inelastic scatterings of the β-electrons on the gas.

Longitudinal inhomogeneities of the source potential are propagated into the model via two parameters and their uncertainties: A potential broadening with variance σ_{z}^2 and a shift of the energy loss function ϵ_{z}. The latter arises as follows: As the source potential shows longitudinal inhomogeneities, the starting potential, which electrons experience, depends on their starting position z in the source. As the scattering and hence energy loss probability is also dependent on the electron's starting position z, the potential gradient can be taken into account by an introduced shift of the energy loss function ϵ_{z}. The broadening is quantified by calibration measurements and can be used to set an upper limit on the energy loss parameter:

$$|\epsilon_{\text{z}}| < \frac{\sigma_{\text{z}}}{\kappa} \tag{3.16}$$

Here κ is an empirical parameter depending on the experimental set-up. Short term fluctuations and a possible long term drift of the plasma potential can be taken into account by considering the variances $\sigma_{\text{s.t.}}^2$ and $\sigma_{\text{l.t.}}^2$ as an additional broadening to the model. In total the plasma related broadening is

$$\sigma_{\text{plasma}} = \sigma_{\text{z}} + \sigma_{\text{s.t.}} + \sigma_{\text{l.t.}}. \tag{3.17}$$

Radial inhomogeneities of the potential can be included into the model via the pixel segmentation of the detector. A radially varying starting potential results in a different retarding potential per pixel. This can be translated into a pixel dependent endpoint E_0 [26, 18].

Background related effects The main background in the KATRIN experiment is proportional to the volume between the analyzing plane and the detector. It can be explained by so called Rydberg electrons, produced by sputtering processes in the spectrometer surface after the analyzing plane. They are then, just as β-electrons with sufficient energy, accelerated towards and counted by the FPD. This background rate is Poisson distributed. Also the FPD itself has an intrinsic Poisson distributed background which is added onto the Rydberg background. Further effects that have to be taken into account individually are the following [18, 27]:

Background energy slope: The background is slightly qU dependent. This is taken into account by describing the background rate $\mathcal{R}_{\mathrm{BG}}$ by a linear function instead of a constant:

$$\mathcal{R}_{\mathrm{BG}}(qU) = \mathcal{R}_{\mathrm{BG}} + m_{\mathrm{BG}} \cdot (qU - E_0) \tag{3.18}$$

With the so called qU-slope m_{BG}. This parameter can be measured using an empty source and then be included in the analysis.

Background overdispersion: Electrons with high transversal energy can be produced and trapped in the main spectrometer due to its magnetic field configuration. They can only escape the spectrometer after losing enough energy via several scatterings. As these scatterings occur related to single trapped electrons the effect is time dependent and hence not Poisson distributed and leads to an overdispersion. This is taken into account by convolving the Poisson-like background model with a Gaussian. The non-Poisson background has the imprint of an increased statistic uncertainty. The effect is eliminated by applying the shifted analyzing plane (SAP) setting.

Penning induced background slope: In measurements where the pre-spectrometer (cf. section 3.1.4) is active, a so called penning trap is formed between the pre- and the main spectrometer. There stored electrons accumulate over time. Positive ions produced here are accelerated into the main spectrometer and cause background electrons. This effect increases until so called penning wipers clean the trap at every step between different retarding potentials. This introduces the additional so called penning slope [28].

Analyzing plane related effects The background rate in the first measurement phases of the KATRIN experiment in 2019 was $\mathcal{O}(20)$ times higher than designed [29]. By shifting the analyzing plane, and hence reducing the volume between the analyzing plane and the detector, the background rate could be reduced by a factor of $\sim$ two. This new shifted analyzing plane (SAP) setting however leads to a larger radial inhomogeneity of the magnetic field B_{ana} and the retarding potential qU. Therefore, the model is split into several patches, while each detector patch combines pixels with similar field values. The SAP setting also leads to a strong potential gradient which introduces another broadening σ^2_{qU}.

The overall shift of qU is translated into the endpoint E_0, as seen for the source potential. However, variations of qU with variance σ^2_{qU} within single pixels are for the shifted analyzing plane (SAP) setting no longer negligible. This effect is treated equivalently to the source potential broadening and their variances are added. The magnetic field in the analyzing plane B_{ana} influences the filter width, and hence the transmission function, just as the magnetic fields mentioned above.

Activity fluctuations Fluctuations of the source activity impact the pre-factor $\mathcal{A}$ from the integral spectrum (eq. 3.14). These changes are known to be small and thus not considered in the neutrino mass analysis.

Molecular final states The theoretical calculation of the FSD does not come with an uncertainty. An uncertainty can only arise from comparing different calculations with one another. This conservative way overestimates the FSD related uncertainty and its treatment in the upcoming neutrino mass analyses is therefore under further discussion [18]. As the impact on the neutrino mass sensitivity is only $\mathcal{O}(10^{-3})$ [29] the FSD uncertainty is not further considered in this thesis.

Detector systematics Some systematic effects arise related to the FPD. The FPD counts for every retarding potential electrons that deposit an energy within a certain region of interest (ROI). The following effects occur [18, 30]:

ROI coverage: As the ROI is not changed depending on the retarding potential, shape distortions can occur, as the fraction of electrons inside the ROI changes for different qU values. Therefore, the detector efficiency ϵ_{FPD} is slightly dependent on the retarding potential qU in terms of a signal-only slope.

Pile-up: The so called pile-up occurs when two or more electrons can temporally not be resolved as single events. They are then counted as one event with the sum of their energies. If this sum exceeds the ROI the events are lost. As this effect increases with the absolute rate, it is also qU dependent. The effect is in general negligible as the systematic uncertainty is $\ll 0.001\,\mathrm{eV}^2$ [30].

Back scattering: Some electrons that hit the detector are back scattered instead of absorbed. If not re-accelerated, they are lost. This effect occurs with a higher probability for lower qU values.

Gain fluctuation: The resolution and gain of the FPD can drift over time. This temporal drift translates non-linearly via the MTD with a maximum distortion around the endpoint.

Chapter 4

Methodology of sensitivity studies

This thesis is dedicated to investigate the final sensitivity of the KATRIN experiment. KATRIN is originally designed to set a limit at 90 % C.L. on the neutrino mass to

$$m_{\nu_e} < 0.2\,\mathrm{eV}(90\ \%\ \mathrm{C.L.}). \tag{4.1}$$

To calculate that sensitivity it is necessary to understand the general neutrino mass analysis approach. This chapter therefore explains the analysis technique in KATRIN (section 4.1). Then the concept of the *sensitivity* is explained (section 4.2) as well as the one of the *discovery potential* (section 4.3).

4.1 Neutrino mass analysis

The neutrino mass analysis is a procedure to determine the value of the neutrino mass m_ν from the data taken with the KATRIN experiment as well as its uncertainty σ_{m_ν}.

4.1.1 Maximum likelihood method

The likelihood (LLH) function $\mathcal{L}(\mu(\boldsymbol{\theta}); x)$ quantifies how well a set of parameters $\boldsymbol{\theta}$ of a certain model μ describes the measured data x for n measurements. Here x is described by a probability mass function (PMF) with a known functional form $f(x; \boldsymbol{\theta})$ [31]:

$$\mathcal{L}(\mu(\boldsymbol{\theta}); x) = \prod_{i=1}^{n} f(x_i; \boldsymbol{\theta}) \tag{4.2}$$

For KATRIN the measured data x is the number of counts N as for each retarding potential qU_i with measurement time t_i the number of counts N_i is measured. The general underlying model μ is the theoretical prediction of the measured counts introduced in 3.2.4 as equation 3.15:

$$\mu(\boldsymbol{\theta}; qU, t) = \left(\mathcal{A} \cdot \int_{qU}^{\infty} \frac{\mathrm{d}\Gamma}{\mathrm{d}E}(E; m_\nu^2, E_0) \cdot \mathcal{R}(E, qU)\mathrm{d}E + \mathcal{B} \right) \cdot t \tag{4.3}$$

The set of parameters $\boldsymbol{\theta}$ to be inferred from the data contains the value of the squared neutrino mass m_ν^2, the endpoint E_0 of the β-spectrum, the normalization factor $\mathcal{A}$ as well as the background rate $\mathcal{B}$:

$$\boldsymbol{\theta} = \{m_\nu^2, E_0, \mathcal{A}, \mathcal{B}\} \tag{4.4}$$

The probability to measure N_i counts assuming the model μ_i is described by the Poissonian PMF

$$f_i(N_i;\mu_i) = \frac{e^{-\mu_i}\cdot \mu_i^{N_i}}{N!}. \tag{4.5}$$

For a large number of counts the PMF can be described as a Gaussian distribution:

$$f_{\mathrm{normal},i}(N_i;\mu_i) = \frac{1}{\sqrt{2\pi N_i}}\exp\left(-\frac{(N_i-\mu_i)^2}{2N_i}\right) \tag{4.6}$$

As the individual measurements i are independent, the joint PMF is the product of the individual Poissonians (or Gaussians):

$$f(N;\mu) = \prod_i f_i(N_i;\mu_i) \tag{4.7}$$

It describes the probability to measure N under the assumption μ. As in practice the measured counts N are known, they are conversely used to infer information on the model μ. This leads to the general KATRIN LLH [18]:

$$\mathcal{L}(\boldsymbol{\theta}, N, qU, t) = \prod_i f(N_i;\mu(\boldsymbol{\theta};qU_i,t_i)). \tag{4.8}$$

This LLH function is maximized by the set of parameters $\boldsymbol{\theta}$ that best describe the data. To provide numerical stability, instead of maximizing the LLH function itself, the negative logarithm of the LLH function (neg. log. LLH) is minimized to infer $\boldsymbol{\theta}$. In the case of a Gaussian PMF the minimization of the neg. log. LLH equals a χ^2 minimization:

$$-2\,\log(\mathcal{L}) = \chi^2 \tag{4.9}$$

Using the maximum LLH method, the measured data can be fitted to obtain the most likely set of parameters $\boldsymbol{\theta} = \{m_\nu^2, E_0, \mathcal{A}, \mathcal{B}\}$ and the related model, together called *best fit*. The obtained χ^2 value and the normalized residuals give an estimation about the goodness of the fit [18]. A fit example is shown in figure 5.3 for unfluctuated Monte Carlo (MC) data.

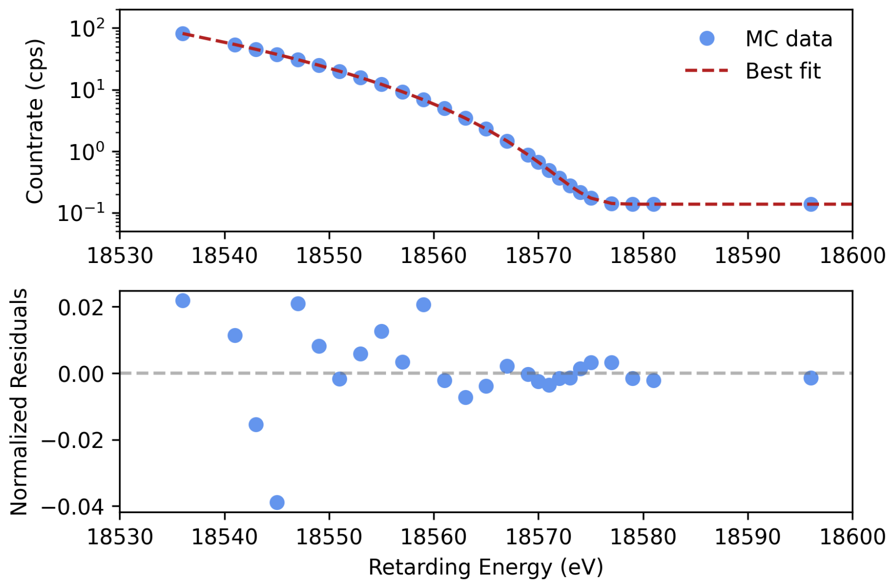

Figure 4.1: Monte Carlo data and best fit from maximum LLH method. The normalized residuals give an estimation about the goodness of the fit.

4.1.2 Data combination

The data, from which the neutrino mass can be inferred, as explained above, is collected in so called β-scans. In between the β-scanning phases however, calibration measurements as well as maintenance have to be done. One continuous β-scanning phase is called a KATRIN neutrino mass (KNM) measurement campaign. In one measurement campaign, all parameters are aimed to be fixed throughout the whole measurement period. Each measurement campaign is split into so called runs while in each run data for every considered retarding potential is taken, according to the MTD. As the measurements are performed with the multi-pixel FPD, the data of all individual pixels has to be combined. Further, also the data of all individual runs and then campaigns is combined to infer one final value for the neutrino mass.

Pixel combination As the spectra taken with individual pixels are independent of one another, the pixel combined LLH is obtained by taking the product over the individual pixel LLHs:

$$\mathcal{L}(\boldsymbol{\theta}, N, qU, t) = \prod_j \prod_i f(N_{i,j}; \mu_{i,j}) \tag{4.10}$$

Here the outer product loops over all pixels (j) and the inner one over the retarding potentials (i). The model μ_j and the parameters $\boldsymbol{\theta}_j$ can differ for each pixel. As it is computationally expensive to calculate the model and do the minimization for each pixel individually, pixels can be grouped together into patches with similar experimental properties. In this case $\prod_j$ in equation 4.10 is the product over all patches. In the case of a single pixel approach, a so called uniform fit, equation 4.8 applies.

Run combination In one measurement campaign the spectrum is measured usually several hundred times in individual runs, according to the same MTD. The run combined LLH is obtained analogously to equation 4.10 by taking the product over all runs s:

$$\mathcal{L}(\boldsymbol{\theta}, N, qU, t) = \prod_s \prod_i f(N_{i,s}; \mu_{i,s}) \tag{4.11}$$

As the experimental parameters can be hold stable throughout a measurement campaign, this procedure can however be avoided as the so called stacked spectrum provides a sufficient approximation. It is built by taking the sum of all counts and measurement times for each voltage set point and averaging over the model parameters.

Combination of measurement campaigns The experimental parameters are often not the same in different measurement campaigns and therefore the before introduced stacking of data is on this level no longer possible. The runs of the individual campaigns remain stacked, but the campaign combined LLH has to consider the product over all campaigns x:

$$\mathcal{L}(\boldsymbol{\theta}, N, qU, t) = \prod_x \prod_i f(N_{i,x}; \mu_{i,x}) \tag{4.12}$$

Combined likelihood The overall combined LLH unites the above introduced concepts: Counts are stacked for runs s within one campaign x and for pixels inside one patch j. Differing experimental parameters between pixels (or patches) and campaigns are accounted for by explicitly combining the individual LLHs [18]:

$$\mathcal{L}(\boldsymbol{\theta}, N, qU, t) = \prod_x \prod_j \prod_i f(N_{x,j,i}; \mu(\boldsymbol{\theta}_{x,j}; qU_{x,j,i}, t_{x,i})) \tag{4.13}$$

4.1.3 Software

Fitrium The `Fitrium` ("fit tritium") software was developed by Dr. Christian Karl. It is written in C++ programming language and provides a model of the tritium β-decay and all relevant parameters of the KATRIN experiment as well as an application for Monte Carlo data generation and for data fitting.

The KATRIN model is built in `Fitrium` following the differential decay rate (eq. 3.7). The model also contains the full response function (eq. 3.13). Therefore the transmission function, the energy loss function and the scattering probabilities are all covered. The FSD is in included via text files. `Fitrium` is described in great detail in [32].

The work presented in this thesis makes use of `Fitrium` in the following way: As different scenarios are investigated, the first step is to generate MC data. `Fitrium` stores the data in an `HDF5` format run summary. A so called run summary in KATRIN contains information about the number of counts, retarding potentials, measurement time and parameters like the magnetic fields or the column density. The underlying model can be configured in an initialization file, called `ini`. Further parameters for the data generation e.g. the considered MTD and the run time are set from the command line. The MTD is read in from a text file, containing information about the fraction of time spent at each qU point. The run time then gets multiplied with that fraction at each qU point. In the second step the generated data is fitted. `Fitrium` reads the information from the run summary and carries out a maximum LLH analysis. The fit results and other meta data is then written to an additional `HDF5` file from where it can be accessed for further investigation and visualization.

To speed up the analysis process, fits with `Fitrium` are only used for cross-checks and the fitting is mainly done using `Netrium`, which is introduced in the following.

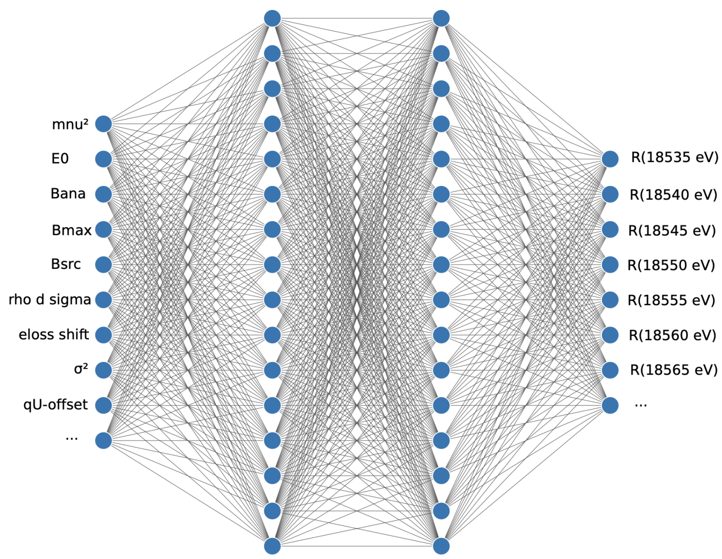

Figure 4.2: Schematic view of the `Netrium` structure. Between the input layer with the physical parameters $\boldsymbol{\theta}$ and the output layer being the learned count rate $\mathcal{R}(qU)$ there are two fully connected hidden layers each with 128 nodes. Figure taken from [18].

Netrium The calculation of the expected rate is computationally involved, as it contains a tremendous amount of summation (e.g. final states in the differential spectrum), root searches (e.g. in the transmission function) and convolutions (e.g. for several scatterings in the energy loss function). These computational demands in combination with the high dimensionality of the parameters $\boldsymbol{\theta}$ to be inferred as well as the high required accuracy bring conventional approaches quickly to the limit of feasibility. To avoid this, a novel approach using a neural net (NN) has been designed. With this new tool, called `Netrium`, a NN is trained with samples generated, following the analytical model. The NN learns the output rate, depending on the physical parameters $\boldsymbol{\theta}$ the spectrum depends on, such as e.g. the squared neutrino mass m_ν^2, the endpoint E_0 and the magnetic fields. Between the input layer (parameters $\boldsymbol{\theta}$) and the output layer (count rate $\mathcal{R}(qU)$) there are two fully connected hidden layers, each with 128 nodes. A schematic view of the `Netrium` structure is shown in figure 4.2.

The training samples are generated covering the expected 1, 3 and 5σ range of each parameter θ. Both a normal and a uniform distribution are considered. The 1σ interval corresponds to the systematic uncertainty or the statistical sensitivity of the respective parameter. Then the integrated spectrum is calculated for the given parameters $\boldsymbol{\theta}$. The full training data set is obtained by repeating this process up to $\mathcal{O}(10^6)$ times.

In the training process a constant background rate is added to the samples and the fraction of all output rates to the sample mean $P_i = \frac{r_i}{\langle r_i \rangle}$ is considered to make sure the net learns the dominant changes. The training is then performed by optimizing the weights ω of the NN to minimize the loss function

$$\mathrm{loss}(\omega) = \left\langle (P_i - P_{\mathrm{pred},i}(\omega))^2 \right\rangle . \tag{4.14}$$

As mentioned above, $P_i = \frac{r_i}{\langle r_i \rangle}$ is the true rate change of each sample and $P_{\mathrm{pred},i}$ the prediction of the net respectively [33, 18].

4.1.4 Treatment of systematic uncertainties

The systematic effects described in 3.3 are considered as additional parameters $\boldsymbol{\theta}_{\mathrm{syst}}$ in the analysis. Each parameter θ_{syst} comes with a central value μ_{syst} and uncertainty σ_{syst}. Usually the parameter uncertainty σ_{syst} is simply a Gaussian standard deviation. There are three common approaches to account for the systematic uncertainties in the analysis process introduced in the following. For further details c.f. [18].

Pull term method In the pull term method the systematic parameters $\boldsymbol{\theta}_{\mathrm{syst}}$ are included in the maximum LLH estimation in addition to the free parameters $\boldsymbol{\theta} = \{m_\nu^2, E_0, \mathcal{A}, \mathcal{B}\}$ as so called Nuisance parameters. The additional PMFs are considered by multiplying the LLH with each of them. By introducing n systematic parameters there are also n new points in the LLH. Hereby the degrees of freedom do not change but an additional width in the parameter interval estimation is introduced. As $\boldsymbol{\theta}_{\mathrm{syst}}$ are included in the LLH learning from the data can occur which can lead to an unrealistic improvement of the uncertainty and a shift of the central value.

Monte Carlo propagation In the MC method data points are sampled randomly (statistics only) according to their PMF. This can also be done with the additional parameters $\boldsymbol{\theta}_{\mathrm{syst}}$ where their PMF describes their systematic uncertainty. This results in a widening of the distribution of the fit parameters. As all fits are performed on MC data, learning from data is not possible as for the Nuisance parameter method.

Covariance matrix approach As the covariance matrix approach makes use of the χ^2 minimization the data must follow a Gaussian PMF. The χ^2 can be expressed as

$$\chi^2 = \sum_i \frac{(N_i - \mu_i)^2}{N_i} = \boldsymbol{r}^T \boldsymbol{V}_{\text{stat}}^{-1} \boldsymbol{r} \tag{4.15}$$

with the residual vector $\boldsymbol{r} = \boldsymbol{N} - \boldsymbol{\mu}$ and the diagonal variance matrix $\boldsymbol{V}_{\text{stat}} = \text{diag}\boldsymbol{N}$. The covariance matrix that describes the systematic uncertainties is obtained by sampling random values of $\boldsymbol{\theta}_{\text{syst}}$ according to their PMF. The prediction for each data point is then evaluated under the corresponding model. The resulting $\boldsymbol{V}_{\text{syst}}$ holds information about the distribution of the model predictions due to the variation of $\boldsymbol{\theta}_{\text{syst}}$. It is then included in the χ^2 from equation 4.15:

$$\chi^2 = \boldsymbol{r}^T (\boldsymbol{V}_{\text{stat}} + \boldsymbol{V}_{\text{syst}})^{-1} \boldsymbol{r} \tag{4.16}$$

4.2 Sensitivity

The sensitivity at a certain Confidence Level (C.L.) of an experiment to the investigated observable, here the sensitivity of KATRIN to the neutrino mass m_ν, is related to an upper limit $L(90\ \%\ \text{C.L.})$. It means that a value (here for the neutrino mass) larger than the obtained limit can be excluded at a 90 % C.L..

4.2.1 Sensitivity goal of the KATRIN experiment

The sensitivity of the KATRIN experiment to the neutrino mass m_ν at 90 % C.L. depends on the uncertainty on m_ν^2. The total uncertainty is given by the quadratic sum of the statistical and the systematic uncertainty:

$$\sigma_{\text{tot}} = \sqrt{\sigma_{\text{stat}}^2 + \sigma_{\text{syst}}^2} \tag{4.17}$$

Under the assumption of a vanishing neutrino mass this total uncertainty defines the upper limit on the neutrino mass as follows:

$$L(90\ \%\ \text{C.L.}) = \sqrt{1.64 \cdot \sigma_{\text{tot}}} \tag{4.18}$$

KATRIN is designed to take data for five calendar years. After the measurements the total uncertainty was originally assumed to be $\sigma_{\text{tot}} \approx 0.025\,\text{eV}^2$. This translates into the goal sensitivity of KATRIN defined by the upper limit [29]

$$m_{\nu_e} < 0.2\,\text{eV}(90\ \%\ \text{C.L.}). \tag{4.19}$$

4.2.2 Analysis of sensitivity scenarios

The work presented in this thesis investigates the final sensitivity of KATRIN under the assumption of different experimental scenarios. Each scenario is realized by simulating a MC data set, considering the respective assumptions on e.g. the experimental parameters, the accuracy of systematic effects or the measurement efficiency. The neutrino mass in this process is fixed to zero. The simulated data is then analyzed as explained in 4.1, yielding a best fit for m_ν as well as an uncertainty σ_{stat} or σ_{tot}, depending on the performed analysis. The uncertainty is then used to estimate the sensitivity that corresponds to the evaluated scenario (c.f. chapter 5), according to equation 4.18.

4.3 Discovery potential

A 3 (or 5)σ discovery potential (D.P.) of φ in KATRIN corresponds to the ability to claim a 3 (or 5)σ discovery, if the final fitted neutrino mass is equal to or larger than φ. In other words, it means that a neutrino mass of φ could be measured with the current set-up and analysis techniques with a residual uncertainty of only 3 (or 5)σ. The D.P. can be calculated in good approximation in analogy to the sensitivity in equation 4.18:

$$\varphi = \sqrt{3(\text{or } 5) \cdot \sigma_{\text{tot}}} \tag{4.20}$$

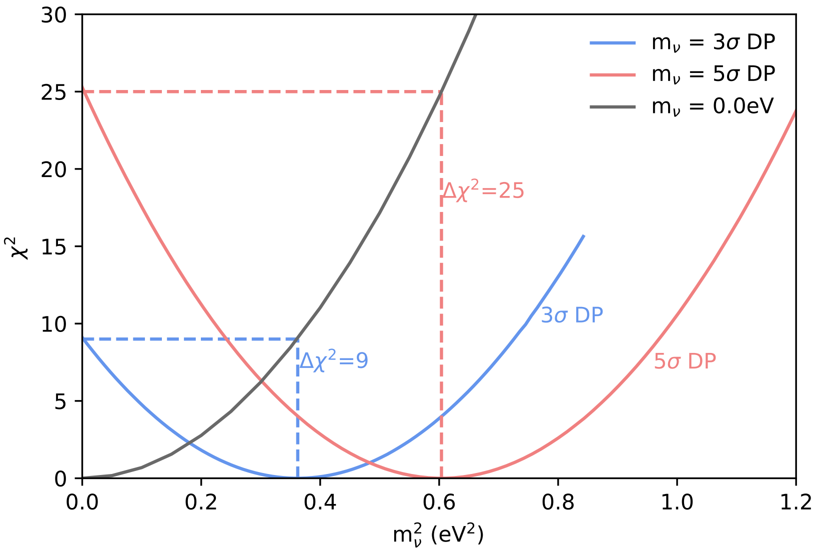

Figure 4.3: Validation of the D.P. calculation approach using a MC data set with neutrino mass set to zero. The black line is the corresponding χ^2 function. The values for the obtained 3 (and 5)σ D.P. correspond to a $3^2 = 9$ and $5^2 = 25$ χ^2 deviation. Considering MC data sets with neutrino masses set to the values of the 3σ D.P. (blue line) and the 5σ D.P. (red line), yield 3 (and 5)σ deviations from the χ^2 minima that correspond to a neutrino mass of $m_\nu = 0$.

4.4 Approach validation

As the approaches, used in this thesis to calculate the sensitivity (eq. 4.18) and the D.P. (eq. 4.20), use MC data with a neutrino mass set to $m_\nu = 0$, they are only approximations. The approach was verified for the calculation of the D.P., and hence as well for the sensitivity, in the course of this thesis in the following way:

- A paradigmatic simulated data set was analysed, as described above, with the true neutrino mass set to zero. The D.P. was then calculated according to eq. 4.20 to $\varphi_{3\sigma} = 0.6019\,\text{eV}$ and $\varphi_{5\sigma} = 0.7771\,\text{eV}$.

- For a first check the χ^2 distribution was calculated. To verify the approach, it was examined if the values for the obtained 3 (and 5)σ D.P. correspond to a $3^2 = 9$ and $5^2 = 25$ χ^2 deviation. This requirement is satisfied as visualized in figure 4.3 (black line).

- A second check was performed by simulating a data set with the true neutrino mass set to $\varphi_{3\sigma} = 0.6019\,\mathrm{eV}$ and to $\varphi_{5\sigma} = 0.7771\,\mathrm{eV}$ respectively. As the 3 (and 5)σ deviations from these χ^2 minima correspond to a neutrino mass of $m_\nu = 0$, the approach to calculate the sensitivity and the D.P. using a MC data set with a neutrino mass set to $m_\nu = 0$ was verified. This is visualized in 4.3 for the 3σ D.P. (blue line) and the 5σ D.P. (red line).

Chapter 5

Sensitivity scenarios

This chapter covers all the sensitivity scenarios that have been investigated in the course of this thesis. The calculation of the sensitivity follows the approach introduced in chapter 4.2. As the scenarios presented here are of hypothetical nature, some baseline assumptions have been made (c.f. 5.2).

5.1 Motivation and overview

As introduced in the previous chapter, KATRIN is designed to set an upper limit on the neutrino mass from β-decay kinematics to

$$m_{\nu_e} < 0.2\,\mathrm{eV}(90\ \%\ \mathrm{C.L.}). \tag{5.1}$$

Now that the experiment has already been taking data for more than four years, the question arises if this sensitivity goal is still realistic or what changes in the current data taking, calibration and analysis methods would have to be made to still reach the goal set back in 2004 [29]. More general, it is of interest to determine the way in which the best final sensitivity possible can be obtained.

Category	**Scenario**	**Chapter**
Previous	2021 projection	5.3.1
	Normal analyzing plane	5.3.2
Signal enhancing	Extended fit range	5.4.1
	Increased acceptance angle	5.4.2
Background reducing	Design background	5.5.1
	aTEF	5.5.2

Table 5.1: Overview of the investigated sensitivity scenarios. They group into scenarios that already took place as well as hypothetical signal enhancing and background reducing scenarios.

The goal sensitivity of 0.2 eV was planned to be obtained by reaching a total uncertainty on the neutrino mass after 1000 days of $\sigma_{\mathrm{tot}} \approx 0.025\,\mathrm{eV}^2$ where $\sigma_{\mathrm{stat}} = \sigma_{\mathrm{syst}} = 0.017\,\mathrm{eV}^2$. Before that, the total uncertainty is dominated by the statistical uncertainty and the sensitivity is thus as well limited by the amount of statistics. Therefore, it is of huge interest to investigate scenarios that would enlarge the amount of data KATRIN can collect in its operation time. The value of interest in this regard is the ratio of signal over background $\frac{\mathcal{S}}{\mathcal{B}}$. This ratio can either be optimized by increasing the signal rate or by decreasing the background rate. Therefore, the scenarios are besides two precedent scenarios (c.f. 5.3) grouped into signal enhancing scenarios (c.f. 5.4) and background reducing scenarios (c.f. 5.5). The studied scenarios are summarized in table 5.1.

5.2 Baseline assumptions

Averaged multi-patch approach The analysis methods introduced in 4.1 are designed to analyze real KATRIN data with one best fit with errors as a result. The full analysis requires precise preparation and as soon as all inputs and parameters are determined correctly, the analysis procedure can still take up to months until a final result is yielded. This is due to the complexity of the KATRIN experiment, its various parameters, the complications the SAP setting introduces and various correlations between different campaigns, parameters and pixels. Using the `Netrium` software to fit the neutrino mass, for each patch one individual net has to be trained, which is a very time consuming task in the process.

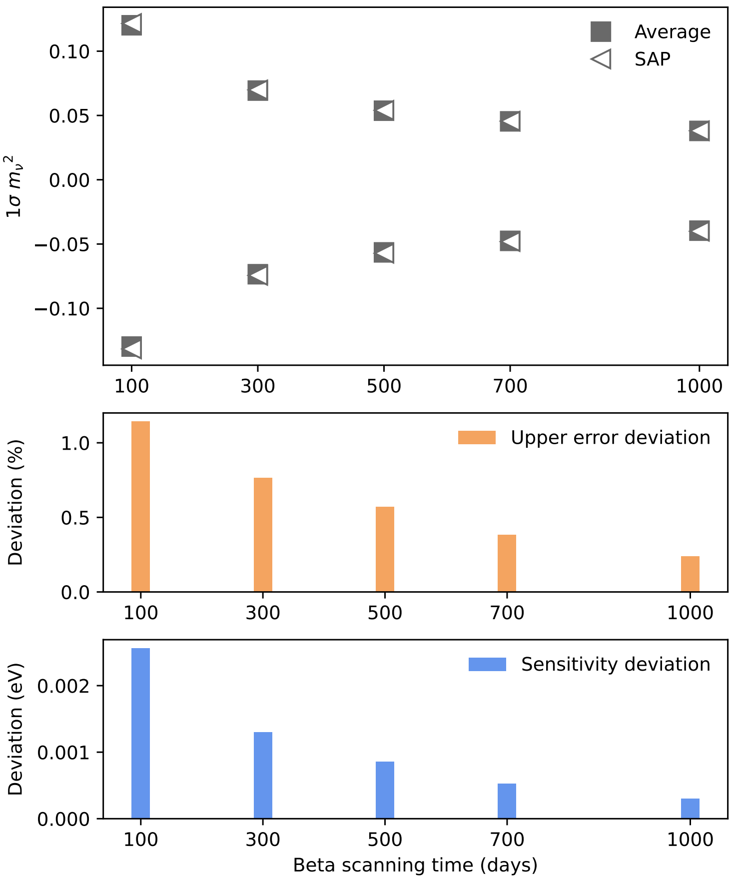

Figure 5.1: Top: Comparison of neutrino mass fit considering the complete SAP setting (white triangles) and an averaged approach (black squares). Middle: The resulting deviation of the upper error on the neutrino mass is $\mathcal{O}(1\%)$. This translates into a deviation of the yielded sensitivity of $\mathcal{O}(0.001\,\text{eV})$.

As the work presented in this thesis covers a variety of mainly hypothetical scenarios, the precise analysis of all of them would have exceeded the overall time frame. Therefore the neutrino mass analysis is slightly simplified. Considering the complete SAP setting would require to perform the analysis process for all commonly defined fourteen patches individually. As mentioned in 4.1.2 in one detector patch several pixels with similar experimental properties are combined. This procedure is avoided in the studies presented in this thesis by considering averaged SAP parameter inputs. Like this only a single fit has to be performed, while not lacking much of the information. Using this approach, only one NN (instead of fourteen) has to be trained for each scenario. To validate this approach the analysis has been performed for an explanatory set of data points using both the regular SAP approach as well as the averaged approach. Both approaches use a Monte Carlo (MC) twin. The twin for the SAP fits is generated with pixel-wise input (one value for each pixel) while the one for the averaged fit is generated considering the inputs averaged over all pixels (one value for all pixels). The inputs used here are the same as in the fifth KATRIN neutrino mass campaign in 2021. The individual fits are then performed considering a single patch with the averaged inputs as well as patch-wise with the individual inputs of the regular fourteen SAP patches (one value for each patch). For these fits the `Fitrium` software has been used.

The results of this validation study are visualized in figure 5.1. When comparing the fit results one sees a deviation of the upper error on the neutrino mass on the order of $\mathcal{O}(1\%)$. As the upper error is used to calculate the sensitivity this directly translates into a deviation of the sensitivity yielded with the different approaches. The deviation in the sensitivity is then on the order of $\mathcal{O}(0.001\,\mathrm{eV})$. This is considered to be accurate enough, as slight changes in the assumptions, from which the individual scenarios arise, easily yield even higher deviations.

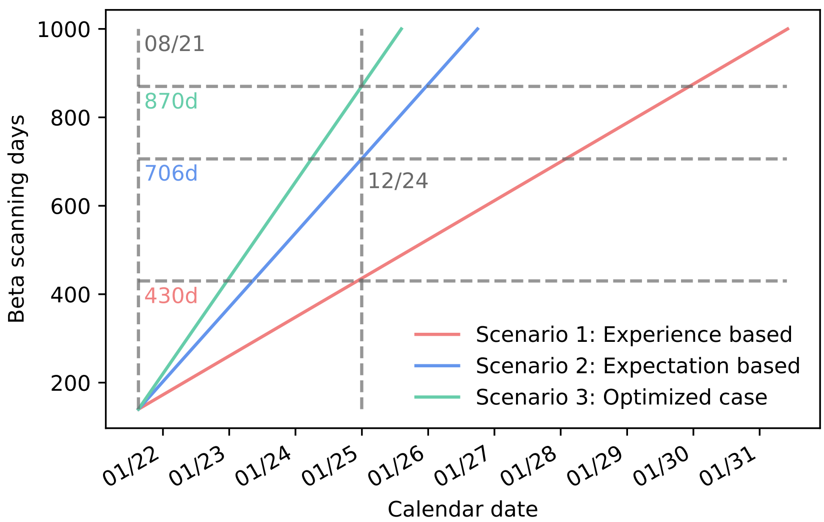

Figure 5.2: Data taking efficiency scenarios: Depending on the time dedicated for β-scanning in one year as well as on the efficiency of the β-scanning itself, after a given time a certain amount of statistics is gained. The visualization starts in August 2021 which marks the start of the sixth KATRIN neutrino mass campaign. At the end of 2024 depending on the underlying considered efficiency scenario 430 full days of statistics (experience based scenario, red line), 706 full days of statistics (expectation based scenario, blue line) or 870 full days of statistics (optimized scenario, green line) are gained. The values shown here are a rough estimate and can therefore slightly differ from the exact results shown later.

Data taking efficiency The general assumption on the data taking efficiency is that per calendar year 210 days are dedicated to the β-scanning. The residual 155 days are for calibration measurements (e.g. with the e-gun) or maintenance. The β-scanning itself has an additional efficiency of here assumed 80 %. This is e.g. due to so called sweeping during the runs as the voltage set points have to be changed according to the MTD and due to the fact that not all runs can in the end be used for the analysis. The described efficiency defines the expectation based scenario, which is mainly used in the following studies. Considering this in one calendar year 168 full days of β-scanning statistics are gained:

$$365\mathrm{d} \cdot \frac{210}{365} \cdot 0.8 = 168\mathrm{d}. \tag{5.2}$$

If another efficiency is considered it is indicated accordingly. To emphasize the impact of the assumed (and in the end reached) data taking efficiency, in figure 5.2 two other scenarios besides the expectation based scenario are visualized. Here the projected sensitivity of the first five measurement campaigns was used to estimate the corresponding amount of statistics. Considering that, the visualization starts in August 2021 which marks the start of the sixth KATRIN neutrino mass campaign after corresponding 140 full days of statistics. At the end of 2024 when KATRIN was originally designed to stop taking data 430 to 870 full days of statistics can be gained depending on the considered efficiency.

Scenario	**β-scan time/year**	**β-scan efficiency**	**statistics/year**
Expectation based	210 days	80 %	168 days
Experience based	131 days	67 %	88 days
Optimized	255 days	85 %	217 days

Table 5.2: Data taking efficiency scenarios.

The assumptions for the individual scenarios are summarized in table 5.2. The expectation based scenario is obtained as described above. The experience based scenario considers the actual efficiency reached in the first five KATRIN neutrino mass campaigns from 2018 to 2021. An additional optimized case would arise if 70 % (255 days) of each year were used for β-scanning, which could only be achieved if nothing besides β-scanning and some maintenance would be performed. Also the β-scanning efficiency itself is with 85 % assumed to be higher than in the other scenarios.

Experimental parameters An individual scenario is mostly defined by the assumed experimental parameters. Therefore they highly vary between the considered scenarios. Different sensitivities arise as soon as e.g. a different analyzing plane set up is considered (shifted analyzing plane (SAP) or normal analyzing plane (NAP)), the background rate differs, or a larger acceptance angle is considered. To clarify the differences, for each sensitivity scenario the assumptions about the underlying parameters are given in the corresponding chapters. Some parameters however stay constant throughout the different scenarios e.g. the detector efficiency, the pixel selection and most of the magnetic field configurations (c.f. table 5.3 and 5.4).

Systematic uncertainties In each scenario the systematic uncertainties are usually held constant, as they are considered as a general underlying assumption just as the experimental parameters. One can however investigate the impact of different systematic uncertainties by varying especially the uncertainty of a single systematic effect to quantify its impact on the overall uncertainty. This can be especially done depending on parameters that quantify the statistics such as the amount of measurement days or the considered fit range (e.g. by expanding it from 40 eV to 90 eV). These investigations are then performed as sub-studies for the corresponding scenarios.

Category	Systematic parameter	Central value	1σ deviation
BG slope	Background slope	2.1 cps/eV	1.2 cps/eV
	BG subrun slope (penning)	0 cps/s	/
CD	Column density ($\rho d\sigma$)	3.769×10^{21}	0.36 %
B-fields	Magnetic field source	2.51 T	0.25 %
	Magnetic field max	4.24 T	0.1 %
RW	Rear wall endpoint (relative)	0 eV	0.1 eV
	Rear wall normalisation	1	0.00005/0.00504
SAP	Magnetic field analyzing plane	0.000548 T	0.72 %
	Transmission broadening	0.02789 eV^2	2.344 %
Plasma	Energy loss shift	0 V	0.02110 V
	Plasma broadening	0.00109 eV^2	0.00019 eV^2
E-loss	Energy loss	current values [20]	current values [20]

Table 5.3: Overview of the assumed systematic effects. They group into 7 effects: The background slope(s), the gas density in the source (column density), the magnetic fields (source and maximum magnetic field), the SAP fields, the source plasma and energy-loss effects. Each parameter is given with its respective 1σ deviation.

Parameter	Value
Analyzing plane	SAP
Background rate	136 mcps
Detector efficiency	95 %
Pixel selection	0-99, 101-111, 114-122, 130-133, 143-144
Endpoint	18573.7 eV
Magnetic field rear wall	1.23 T
Endpoint rear wall	18575.29 eV
Rear wall normalization	0.00504
Source Temperature	78.85 K
Normalization	1.16
Magnetic field transport	3.6 T
Retarding energy offset	-7.424 eV
Non-Poisson background	/

Table 5.4: Overview of the assumed experimental parameters. These also define the scenario but are not considered for the estimation of the systematic error on the neutrino mass. Especially the background rate has a large impact on the sensitivity.

General parameters As mentioned above, the individual scenarios are defined by the assumed parameters. Many of them however stay constant for all scenarios. Table tables 5.3 and 5.4 give a detailed overview over all considered parameters in the data generation and analysis. The parameters shown here are the averaged values of the fifth KATRIN neutrino mass campaign which is mostly used as a reference. Whenever a systematic or experimental parameter differs from the here shown it is indicated accordingly.

Correlation between systematic parameters As some systematic effects have an impact on several parameters, the correlation between these parameters has to be taken into account in the analysis via covariance matrices. This is shown for the case of the SAP-fields systematic. The SAP setting introduces an additional broadening to the spectrum called transmission broadening. The uncertainty on this additional broadening now correlates with the uncertainty on the magnetic field in the analyzing plane. The individual 1σ uncertainties as well as the strength of the correlation are quantized in the covariance matrix in the following way:

$$\mathcal{C} = \begin{pmatrix} \sigma_1^2 & \rho \cdot \sigma_1 \cdot \sigma_2 \\ \rho \cdot \sigma_1 \cdot \sigma_2 & \sigma_2^2 \end{pmatrix} \tag{5.3}$$

with usually $\rho = -0.24$ the strength of the correlation, $\sigma_1 = \sigma_{B_{\text{ana}}}$ the uncertainty on the magnetic field in the analyzing plane and $\sigma_2 = \sigma_{\sigma^2_{\text{trans}}}$ the uncertainty on the squared transmission broadening.

As soon as also the uncertainty for the plasma broadening is considered the co-variance matrix has to be extended as both the plasma and the SAP-fields have an impact on the broadening of the spectrum:

$$\mathcal{C} = \begin{pmatrix} \sigma_1^2 & \rho \cdot \sigma_1 \cdot \sigma_2 \\ \rho \cdot \sigma_1 \cdot \sigma_2 & \sigma_2^2 \end{pmatrix} + \begin{pmatrix} 0 & 0 \\ 0 & \sigma_3^2 \end{pmatrix} \tag{5.4}$$

with $\sigma_3 = \sigma_{\sigma^2_{\text{plasma}}}$ the uncertainty on the squared plasma broadening.

The energy-loss is defined by 9 parameters. Therefore the regarding covariance matrix is of the shape 9×9. The respective values come from measurements [20].

Data simulation and neural net For all scenarios a MC data set is simulated using the `Fitrium` software. This is then handled as a regular KATRIN run summary. As a cross-check the simulated data can be fitted also using `Fitrium`. To make use of `Netrium` the corresponding NN has to be trained. This is done in the following steps:

- Define parameter inputs with central value and standard deviation for each parameter to cover the whole needed parameter space for the analysis.
- Generate the training samples. In this step the model is evaluated very often for different parameter values up to 5σ deviation.
- Train the NN. In this procedure the samples are read in from files, the data is split into training and validation samples and then the model is trained. In the course of the training the minimizer tolerance is gradually decreased yielding one final model that is used for the analysis.

5.3 Current and previous scenarios

The first two scenarios presented here are built from measurements that actually took place in the past. The *2021 projection* relies on parameters that were present in the fifth measurement campaign. This scenario is assumed to be representative also for future campaigns and is therefore considered as the most accurate projection for the final KATRIN sensitivity. The *normal analyzing plane* scenario reproduces the setting that was present before the shifted analyzing plane (SAP) setting was used. Also in this scenario projections to a final KATRIN sensitivity are made, mostly to stress the benefit the SAP setting brought.

5.3.1 2021 projection

After the fifth KATRIN neutrino mass campaign in 2021, the sensitivity from statistics only analyses is projected to be at 0.42 eV [34]. A result is planned to be published soon this year. The following campaign then started in August 2021. The *2021 projection* scenario therefore assumes as a starting point for further estimations a statistics only sensitivity of 0.42 eV in August 2021. The scenario is built assuming the systematics and further parameters that were present in the fifth campaign as these parameters are estimated to be representative also for future campaigns. The parameters defining this scenario are exactly the ones from table 5.3 and 5.4. Only the systematic uncertainty on the gas density in the source, the so called column density $\rho d\sigma$ is varied within the study. It was originally assumed to be at ±0.16% but is now considered as ±0.36% for the final neutrino mass analysis.

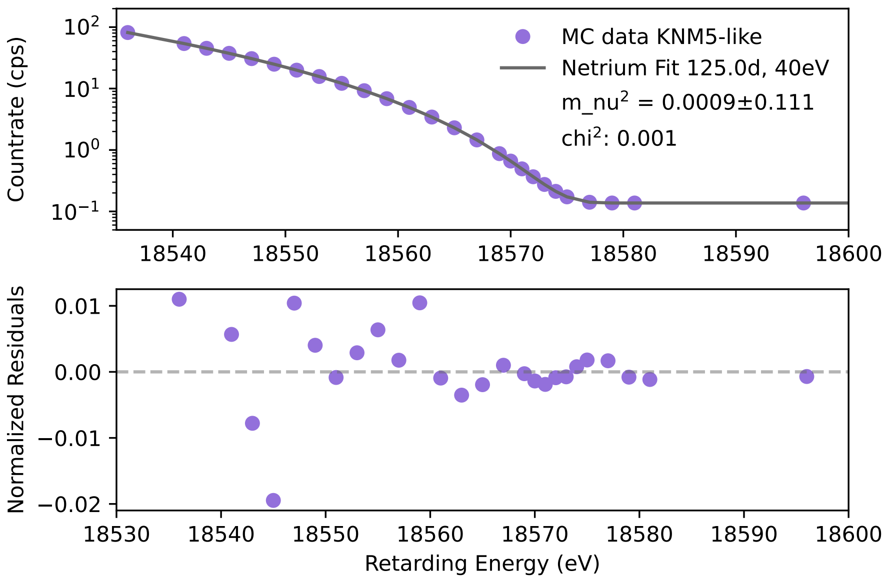

Figure 5.3: `Netrium` fit evaluating the 40 eV fit range for 125 days of statistics. It yields a best fit result of $m_\nu = (0.000\,89 \pm 0.110\,90)\,\mathrm{eV}^2$. The upper error of $\sigma_{\mathrm{upper}} = 0.1077\,\mathrm{eV}^2$ yields the statistics only sensitivity of 0.42 eV.

The statistics only sensitivity of 0.42 eV is reached assuming the introduced scenario after 125 full measurement days. This data point is then defined as August 2021: after that the conversion between measurement days and calender time is made as introduced in equation 5.2 (1 year ≡ 168 full β-days). The corresponding `Netrium` fit is shown in figure

5.3. Evaluating the 40 eV fit range for 125 days of statistics yields a best fit result of $m_\nu = (0.000\,89 \pm 0.110\,90)\,\mathrm{eV}^2$. The 1σ uncertainty is calculated from the upper and lower error: $(\sigma_{\mathrm{upper}} + \sigma_{\mathrm{lower}})/2$. The upper error of $\sigma_{\mathrm{upper}} = 0.1077\,\mathrm{eV}^2$ yields the sensitivity of interest.

Statistics only

The statistics only sensitivity evaluation is then performed for data points up to the end of 2029. At the end of 2024, when KATRIN was originally designed to stop taking data, 700 full days of statistics could be collected assuming the here investigated scenario. This would yield a sensitivity of $m_{\nu_e}(700\text{ d, stat. only}) < 0.27\,\mathrm{eV}(90\ \%\ \mathrm{C.L.})$. The final 1000 days of statistics could be gained under the assumed conditions in late 2026 with a sensitivity of $m_{\nu_e}(1000\text{ d, stat. only}) < 0.25\,\mathrm{eV}(90\ \%\ \mathrm{C.L.})$. The statistics only sensitivity curve is visualized in figure 5.4.

Here is to note that the 125 days needed to reach 0.42 eV assume the here presented 2021 projection. In reality the collected days of statistics slightly differ from that value, as the first four measurement campaigns showed different properties. The 125 here presented days in the assumed scenario correspond to ~ 205 full days gained in the first five campaigns. If one would therefore consider this way of counting at the end of 2024 already ~ 780 days are collected and 1000 days would refer to earlier in 2026. The sensitivity would however not change, as the first days were less efficient in minimizing the sensitivity than the here presented scenario (because of higher backgrounds etcetera).

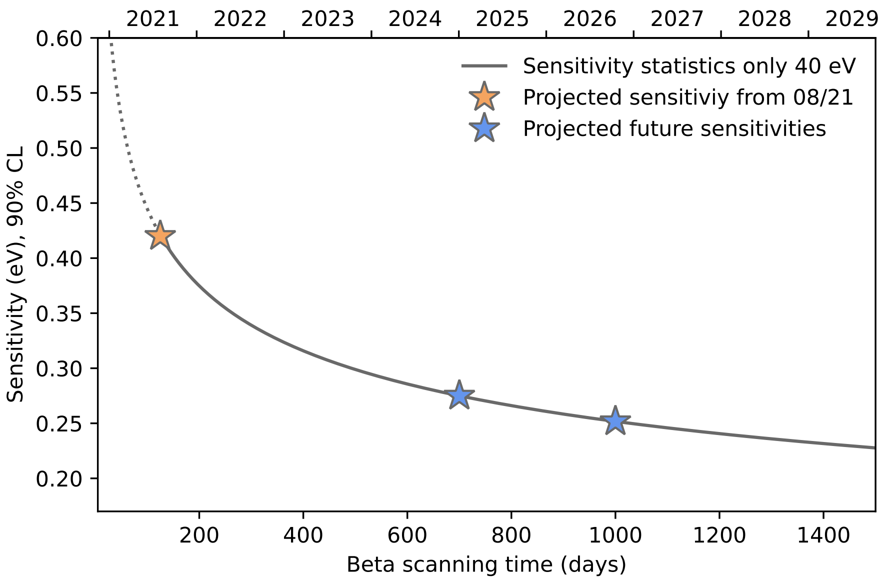

Figure 5.4: Sensitivity projection (statistics only) assuming parameters of the fifth KATRIN campaign and evaluation in the 40 eV fitrange. The starting point is set to August 2021 where after the analysis of the fifth measurement campaign a sensitivity of 0.42 eV can be anticipated (yellow star). At the end of 2024 assuming the here investigated scenario 700 full days of statistics could be collected . This would yield a sensitivity of $m_{\nu_e}(700\text{ d, stat. only}) < 0.27\,\mathrm{eV}(90\ \%\ \mathrm{C.L.})$. The final 1000 days of statistics would be gained in late 2026 with a sensitivity of $m_{\nu_e}(1000\text{ d, stat. only}) < 0.25\,\mathrm{eV}(90\ \%\ \mathrm{C.L.})$ (blue stars).

Statistics and systematics combined

For the statistics only evaluation the starting point has been set to the projected sensitivity of 0.42 eV in August 2021 after corresponding 125 days of statistics. If now the sensitivity considering also the systematic uncertainty is investigated this starting sensitivity shifts to respective 0.43 eV. This was presented in [34] and could be reproduced performing a `Netrium` total fit considering 125 days of statistics.

Calculating the sensitivity from the error on the neutrino mass considering the total uncertainty (statistical uncertainty and all uncertainties introduced by systematic effects) yields the following results: At the end of 2024 (after 700 full days) $m_{\nu_e}(700\text{ d, total}) < 0.30\,\text{eV}(90\ \%\ \text{C.L.})$ can be reached. After 1000 full days (late 2026) $m_{\nu_e}(1000\text{ d, total}) < 0.29\,\text{eV}(90\ \%\ \text{C.L.})$ could be reached. These values as well as the ones for the statistics only case are summarized in table 5.5.

Type	**August 2021**	**End 2024**	**Late 2026**
Statistics	0.42 eV	0.27 eV	0.25 eV
Total	0.43 eV	0.30 eV	0.29 eV

Table 5.5: Sensitivity (statistics only and total) in August 2021, after 700 days of statistics (end 2024) and 1000 days (late 2026).

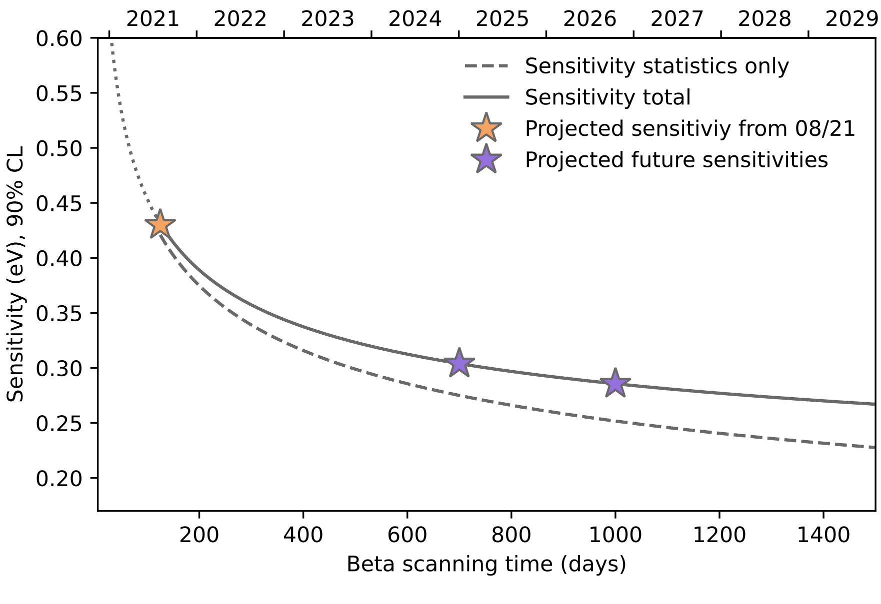

Figure 5.5: Sensitivity projection (total) assuming parameters of the fifth KATRIN campaign and evaluation in the 40 eV fitrange. The starting point is set to August 2021 where after the analysis of the fifth measurement campaign a sensitivity of 0.43 eV can be anticipated (yellow star). At the end of 2024 assuming the here investigated scenario 700 full days of statistics could be collected. This would yield a sensitivity of $m_{\nu_e}(700\text{ d, total}) < 0.30\,\text{eV}(90\ \%\ \text{C.L.})$. The final 1000 days of statistics would be gained in late 2026 with a sensitivity of $m_{\nu_e}(1000\text{ d, total}) < 0.29\,\text{eV}(90\ \%\ \text{C.L.})$ (purple stars). The dashed line shows the statistics only sensitivity from figure 5.4 as a reference.

Systematics breakdown end 2024

To show the impact on the neutrino mass sensitivity of all individual systematic effects, a systematics breakdown is performed. In that process the impact of the individual systematic uncertainties is calculated by quadratic subtraction. This is here done for 700 full days of statistics, as that represents the amount of data that will probably be gained by the end of 2024. The total uncertainty at the end of 2024 is projected to be $0.057\,\mathrm{eV}^2$. To that value the statistical uncertainty contributes with $0.047\,\mathrm{eV}^2$ and all systematics combined with $0.033\,\mathrm{eV}^2$. KATRIN is hence still going to be limited by the statistical uncertainty. The impact of all individual systematic effects is shown in figure 5.6. All systematic effects are considered with the uncertainties shown in table 5.3. The column density uncertainty is assumed to be $\pm 0.36\%$.

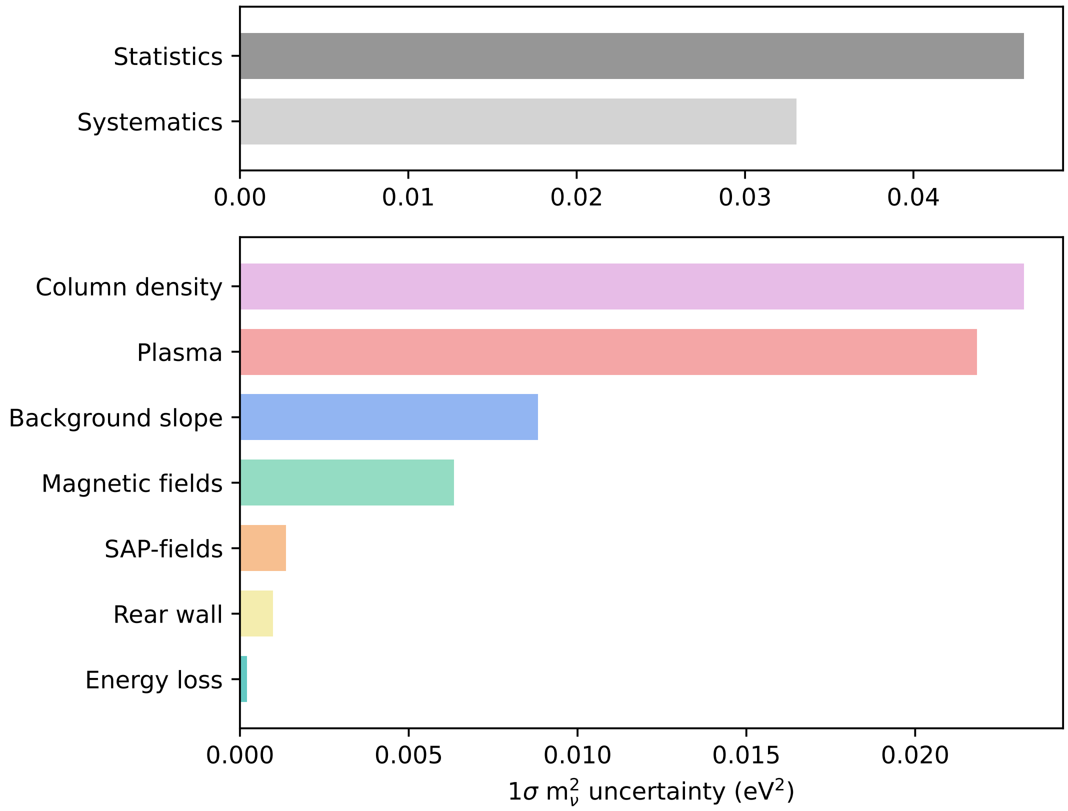

Figure 5.6: Systematics breakdown for the 2021 projection. The bars quantize the 1σ uncertainty on the squared neutrino mass. The individual values are: statistics (dark grey): $0.047\,\mathrm{eV}^2$, all systematics combined (light grey) $0.033\,\mathrm{eV}^2$, column density (pink) $0.023\,\mathrm{eV}^2$, plasma (red): $0.022\,\mathrm{eV}^2$, background slope (blue): $0.009\,\mathrm{eV}^2$, magnetic fields (green): $0.006\,\mathrm{eV}^2$, SAP-fields (orange): $0.001\,\mathrm{eV}^2$, rear wall (yellow): $0.001\,\mathrm{eV}^2$, energy loss (turquoise): negligible in the here performed analysis. Mind the different scale on the x-axis in the top and bottom graph.

Impact of column density uncertainty

As seen in figure 5.6, the uncertainty on the column density acts as the largest constraint on the sensitivity, as it comes with the largest error on the neutrino mass compared to all other systematic effects. Here the respective uncertainty is considered as $\pm$ 0.36%

translating into an error of $0.023\,\mathrm{eV}^2$, but originally it was assumed that the column density could be determined more accurately especially via e-gun measurements. As it showed, there was however an unaccounted bias in the calibration procedure. Therefore the uncertainty increased and was investigated thoroughly over the past years [35]. To investigate the impact of a varying column density uncertainty, the analysis has been repeated for different values. The yielded profile is shown in figure 5.7a. As stated above, the now assumed to be realistic uncertainty of $\pm 0.36\%$ translates into an additional 1σ uncertainty on m_ν^2 of $0.023\,\mathrm{eV}^2$. If the considered uncertainty is $\pm 0.10\%$ the error is $0.007\,\mathrm{eV}^2$ and for $\pm 1.00\%$ the error is $0.042\,\mathrm{eV}^2$ respectively.

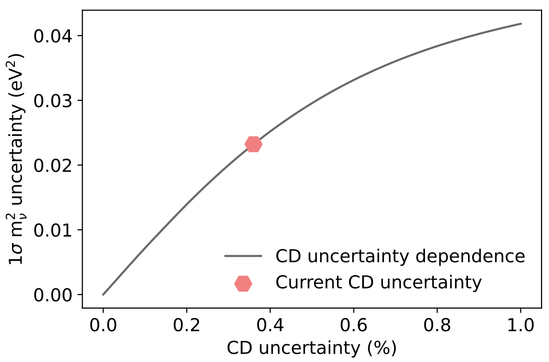

(a) Profile of the dependence of the 1σ uncertainty on m_ν^2 on the column density uncertainty. The now assumed to be realistic uncertainty of $\pm 0.36\%$ translates into an additional 1σ uncertainty on m_ν^2 of $0.023\,\mathrm{eV}^2$. If the considered uncertainty is $\pm 0.10\%$ the error is $0.007\,\mathrm{eV}^2$ and for $\pm 1.00\%$ the error is $0.042\,\mathrm{eV}^2$ respectively.

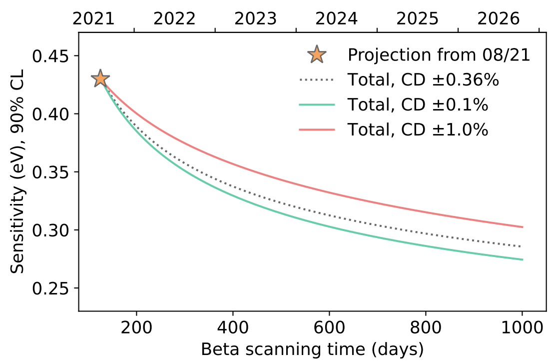

(b) Impact of the column density uncertainty on the total KATRIN sensitivity on the neutrino mass. For an assumed CD uncertainty of $\pm 0.10\%(\pm 1.00\%)$ the sensitivity at the end of 2024 is $0.29\,\mathrm{eV}(0.32\,\mathrm{eV})$ and after 1000 days of statistics $0.27\,\mathrm{eV}(0.30\,\mathrm{eV})$. Green line: $\pm 0.10\%$ and red line: $\pm 1.00\%$. Grey dotted line: $\pm 0.36\%$ as a reference.

Figure 5.7: Impact of column density uncertainty on the additional error on the squared neutrino mass (a) and on the sensitivity (b).

The differing additional error caused by a varied column density uncertainty directly translates into different sensitivity results. This effect is shown in figure 5.7b. For an assumed column density uncertainty of $\pm 0.10\%$ the sensitivity at the end of 2024 is $0.29\,\mathrm{eV}$ and after 1000 days of statistics $0.27\,\mathrm{eV}$ (green line). For an uncertainty of $\pm 1.00\%$ the sensitivity at the end of 2024 is $0.32\,\mathrm{eV}$ and after 1000 days of statistics $0.30\,\mathrm{eV}$ respectively (red line). The reachable sensitivity results are summarized in table 5.6 for different column density uncertainties. To obtain the same starting point of $0.43\,\mathrm{eV}$ in August 2021 the red curve is shifted by forty days compared to the one in figure 5.5 that assumes $\pm 0.36\%$ and the green curve is shifted by minus five days.

CD uncertainty	**End 2024 (700 days)**	**Late 2026 (1000 days)**
0.10%	0.29 eV	0.27 eV
0.36%	0.30 eV	0.29 eV
1.00%	0.32 eV	0.30 eV

Table 5.6: Sensitivity dependence on the column density uncertainty. All sensitivities shown consider the total uncertainty including the respective uncertainty on the column density.

5.3.2 Normal analyzing plane

Before the shifted analyzing plane (SAP) setting was applied all measurements were taken in the normal analyzing plane (NAP) setting. By changing the setting the background could be reduced by around 100 mcps (millicounts per second). The downside of this change was however that now the analysis has to be performed patch wise, as many parameters now show increased inhomogeneities at the detector. The here presented study was performed to estimate the sensitivity improvement the introduced SAP setting brought. Therefore, here the NAP setting is considered as in the first KATRIN neutrino mass campaigns. Some effects however are considered to be improved. For example the pre-spectrometer is also considered to be shut off and hence there is no penning background. The main differences compared to the 2021 projection scenario are an increased background rate of 220 mcps, an additional non-Poisson background (cf. background overdispersion in 3.3) and no additional transmission broadening. All settings used to build the NAP scenario are summarized in table 5.7 and 5.8.

The fist two KATRIN neutrino mass campaigns yielded a combined total sensitivity of $m_{\nu_e} < 0.8\,\mathrm{eV}$(90 % C.L.). This was reached with the data taken until fall 2019. The subsequent measurement campaign started in June 2020. This corresponds in the here presented scenario to 20 full days of statistics. Note that this is less than a simulation of the actual first two campaigns would have yielded, as here better conditions are assumed (e.g. no penning background). To be now able to compare the NAP setting to the SAP setting the same data taking efficiency is assumed for both scenarios between June 2020 and August 2021: The experience based data taking efficiency from table 5.2 of 24% (88 days per calendar year). Under this assumption between the two dates of interest 115 days of β-data could be collected. Examining the SAP simulations yields the same result as with the SAP data 0.8 eV can already be reached after 10 days. As seen before, 0.43 eV are then reached after 125 days and the difference is the corresponding 115 days. In the NAP scenario August 2021 thus corresponds to 135 full days of statistics. These yield a sensitivity of 0.51 eV compared to the 0.43 eV for the SAP.

Category	Systematic parameter	Central value	1σ deviation
BG slope	Background slope	0 cps/eV	1.2 cps/eV
	BG subrun slope (penning)	0 cps/s	/
CD	Column density ($\rho d\sigma$)	3.771×10^{21}	0.36 %
B-fields	Magnetic field source	2.51 T	0.25 %
	Magnetic field max	4.24 T	0.1 %
	Magnetic field analyzing plane	0.000629 T	0.72 %
RW	Rear wall endpoint (relative)	0 eV	0.1 eV
	Rear wall normalization	1	0.00002/0.01
Plasma	Energy loss shift	0 V	0.02110 V
	Plasma broadening	0.00089 eV^2	0.00019 eV^2
	Endpoint broadening	-0.001597 eV^2	0.000773 eV^2
E-loss	Energy loss	current values [20]	current values [20]

Table 5.7: Overview of the assumed systematic effects for the NAP scenario. Each parameter is given with its respective 1σ deviation.

Parameter	Value
Analyzing plane	NAP
Background rate	220 mcps
Detector efficiency	95 %
Pixel selection	0-99, 101-111, 114-122, 130-133, 143-144
Endpoint	18573.7 eV
Magnetic field rear wall	1.23 T
Endpoint rear wall	18575.22 eV
Rear wall normalization	0.01
Source Temperature	78.85 K
Normalization	1.0
Magnetic field transport	3.6 T
Retarding energy offset	-1.90188 eV
Non-Poisson background	0.01178983 cps

Table 5.8: Overview of the assumed experimental parameters. Especially the higher background rate and the additional non-Poisson background (background overdispersion) define the NAP scenario.

Starting from August 2021, again the expected data taking efficiency of 46% (168 days per year) is assumed. The corresponding sensitivity curve considering the NAP scenario is shown in figure 5.8 (blue line). As mentioned above the total sensitivity reachable by August 2021 is 0.51 eV. By the end of 2024 a sensitivity of 0.36 eV can be reached and after 1000 full days 0.33 eV. August 2021 and the end of 2024 are marked with a grey line. Also shown in figure 5.8 are the statistics only curve (black line) and the impact of the non-Poisson background (black dashed line). The latter is investigated in more detail at the end of this chapter.

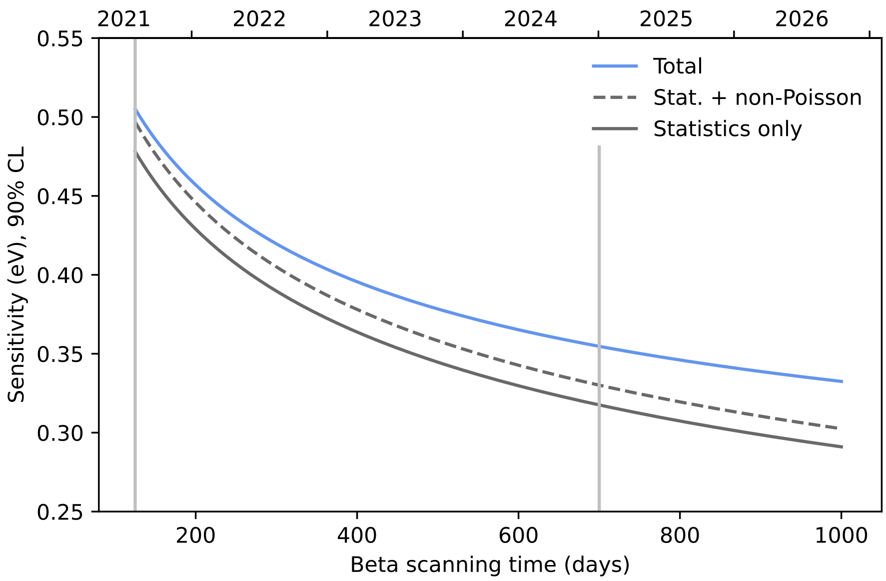

Figure 5.8: Sensitivity curves assuming the NAP scenario. Total sensitivity: Blue line, Statistics only: black solid line, statistics incl. non-Poisson background: black dashed line. August 2021 and the end of 2024 are marked with a grey line.

The comparison between the sensitivity prospect of measurements taken in the NAP and the SAP setting is shown in figure 5.9. With the data taken until August 2021 in the SAP setting (green line) already a sensitivity of 0.43 eV is reachable. In the NAP setting (blue line) this would only be reached after additional 10 months (140 measurement days) in June 2022. At the end of 2024 the sensitivity yielded with the SAP setting is 0.06 eV better than with the NAP setting and in late 2026 the improvement would still be around 0.04 eV. A fit range extension (for more detail cf. chapter 5.4.1) to 60 eV (blue dashed line) would only yield a sensitivity improvement of 7 meV by the end of 2024 compared to the 40 eV fit range and even less for more statistics. The respective sensitivities are summarized in table 5.9.

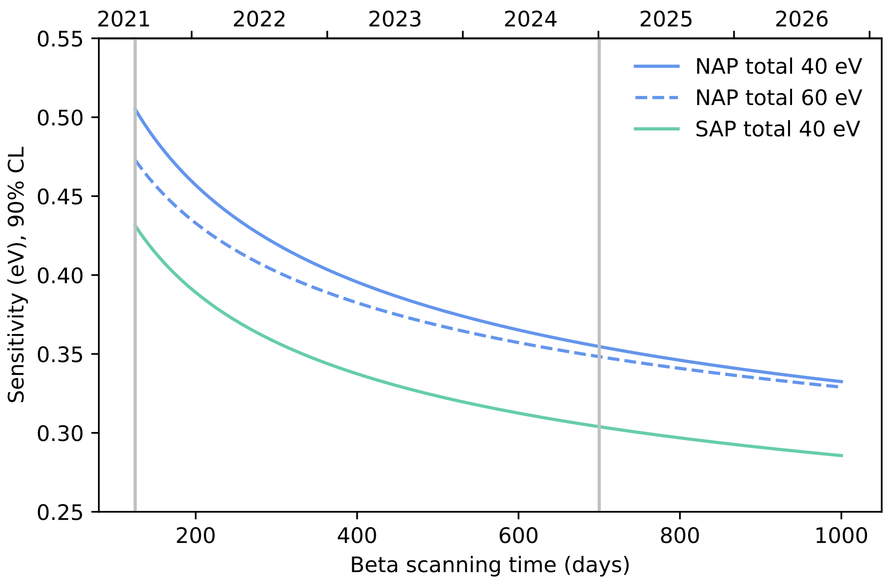

Figure 5.9: Comparison of NAP and SAP sensitivity. Measuring in the SAP setting (green line) yields at the end of 2024 a 0.06 eV better sensitivity than in the NAP setting (blue solid line). Extending to the 60 eV fit range (blue dashed line) would only bring an improvement in sensitivity of 7 meV by the end of 2024 compared to the 40 eV fit range. August 2021 and the end of 2024 are marked with a grey line.

Scenario	**2021 (125 d)**	**2024 (700 d)**	**2026 (1000 d)**
NAP 40 eV	0.51 eV	0.36 eV	0.33 eV
NAP 60 eV	0.47 eV	0.35 eV	0.33 eV
SAP 40 eV	0.43 eV	0.30 eV	0.29 eV

Table 5.9: Sensitivity prospect for the NAP and SAP setting. For NAP also an extension to 60 eV is considered.

As introduced before, in the NAP setting an additional non-Poisson background occurs. This background, also called background overdispersion, is due to electrons trapped in the main spectrometer that can only escape and reach the detector after several scatterings. As introduced in chapter 3.3 the non-Poisson background is observed as an increased statistical uncertainty. In figure 5.10 the impact of the non-Poisson background compared to the impact of systematic effects is visualized. The top plot shows the 1σ uncertainty on m_ν^2 for the statistics only case (dashed line), for statistics including the non-Poisson background (dotted line) and for the total case also accounting for all systematic effects (solid line). The graph in the middle shows the 1σ uncertainty on m_ν^2 caused by the statistics, the non-Poisson background and the systematics individually. In the bottom graph the relative impact of the non-Poisson background (dashed red line) as well as all systematics combined (dashed blue line) can be seen. The non-Poisson background establishes as a constant additional statistical uncertainty of 42% compared to the regular statistical uncertainty. The relative impact of the systematic uncertainty compared to the statistical uncertainty increases over time. This is due to the fact that the statistical uncertainty itself decreases for a higher amount of statistics.

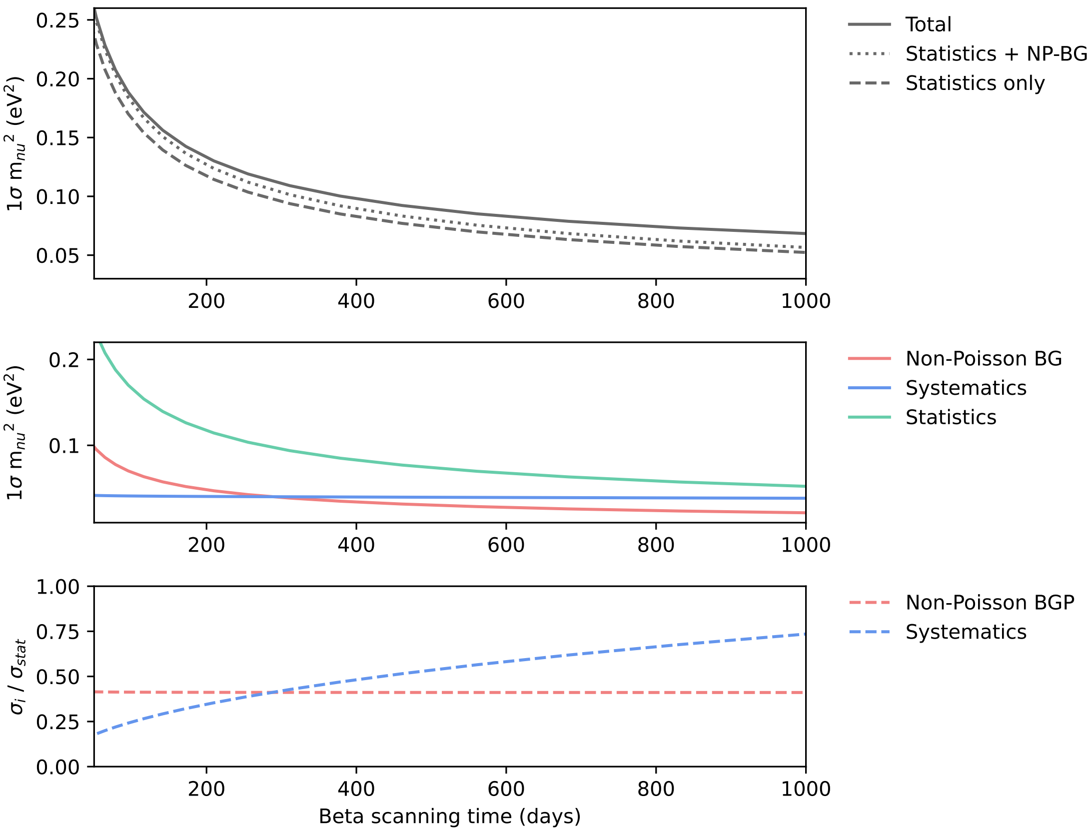

Figure 5.10: Impact of non-Poisson background. Top: 1σ uncertainty on m_ν^2 for the statistical uncertainty (dashed line), the statistical uncertainty including the non-Poisson background (dotted line) and the total uncertainty when considering statistics, the non-Poisson background and all systematic effects (solid line). Middle: 1σ on m_ν^2 due to statistics only (green line), due to the non-Poisson background only (red line) and due to the systematic effects only (blue line). Bottom: Relative impact of the non-Poisson background (red dashed line) and of systematic effects (blue dashed line) to the statistical uncertainty.

5.4 Signal enhancing scenarios

The motivation for investigating signal enhancing scenarios is on the one hand to improve the ratio of signal over background $\frac{S}{B}$. As the background is produced in other processes than the signal β-electrons a signal enhancement does not necessarily come with a larger background. On the other hand KATRIN is also in the future going to be dominated by the statistical uncertainty as seen in figure 5.6. Therefore it is aimed to increase the amount of statistics that can be collected in the same time. In this regard the effects of an extended fit range and an increased acceptance angle are investigated in the following.

5.4.1 Extended fit range

In the regular neutrino mass analysis the β-spectrum is investigated down to 40 eV below the endpoint. In this 40 eV fit range the data from 22 retarding energy set points is considered (between 18 535.5 keV and 18 575.5 keV). Data is taken however up to 91 eV below the endpoint [22]. In the 90 eV fit range 9 additional retarding energy set points are considered. Figure 5.11 shows a `Netrium` fit with 90 eV fit range considered for 125 days of data in analogy to 5.3 for the 40 eV fit range. The rate deeper in the spectrum increases according to the transmission function for smaller retarding energies. Therefore, for the same data taking time the amount of gained statistics increases. Some systematic effects however, especially the ones connected to scattering effects, are harder to describe and hence their uncertainty increases as well. The study presented in the following, investigates if a fit range extension up to 60 eV or 90 eV would yield a sensitivity improvement. Also here the impact of the column density uncertainty is examined. It increases deeper in the spectrum, as more scattered electrons are considered. Also the uncertainty coming with the FSD increases for an extended fit range. This is however not included in the performed study.

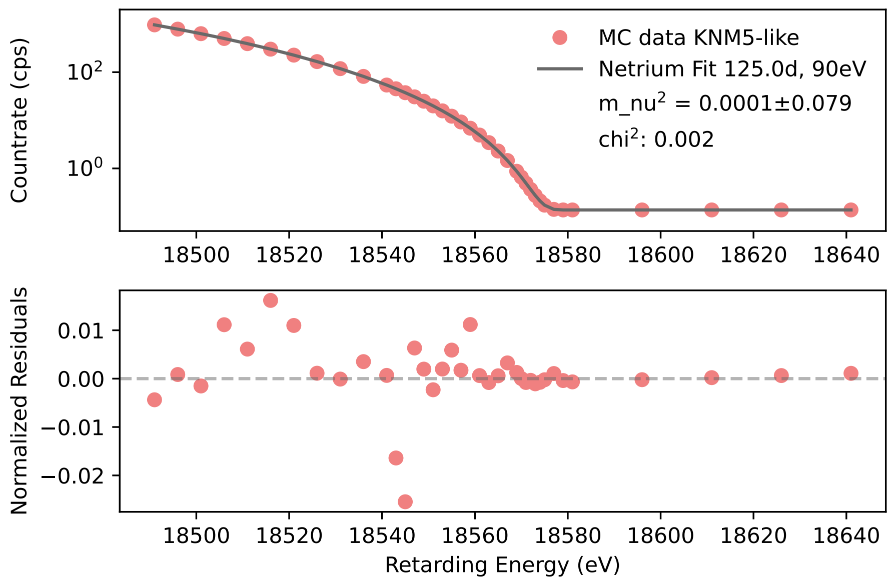

Figure 5.11: `Netrium` fit evaluating the 90 eV fit range for 125 days of statistics. It yields a sensitivity of 0.36 eV.

The here presented study uses the same simulated data and systematic assumptions as the 2021 projection in chapter 5.3.1. As the fit range extension directly increases the amount of statistics, it is obvious that the statistics only sensitivity improves. This is shown in figure 5.12. In chapter 5.3.1 0.42 eV are used as the sensitivity one could reach with data until August 2021. This point is here again assumed for the analysis considering the 40 eV fit range (125 days). If the analysis would be repeated considering a larger fit range this could be improved. Therefore for all investigations with different fit ranges 125 days of statistics are here simply set to August 2021 without shifting the respective sensitivity curves.

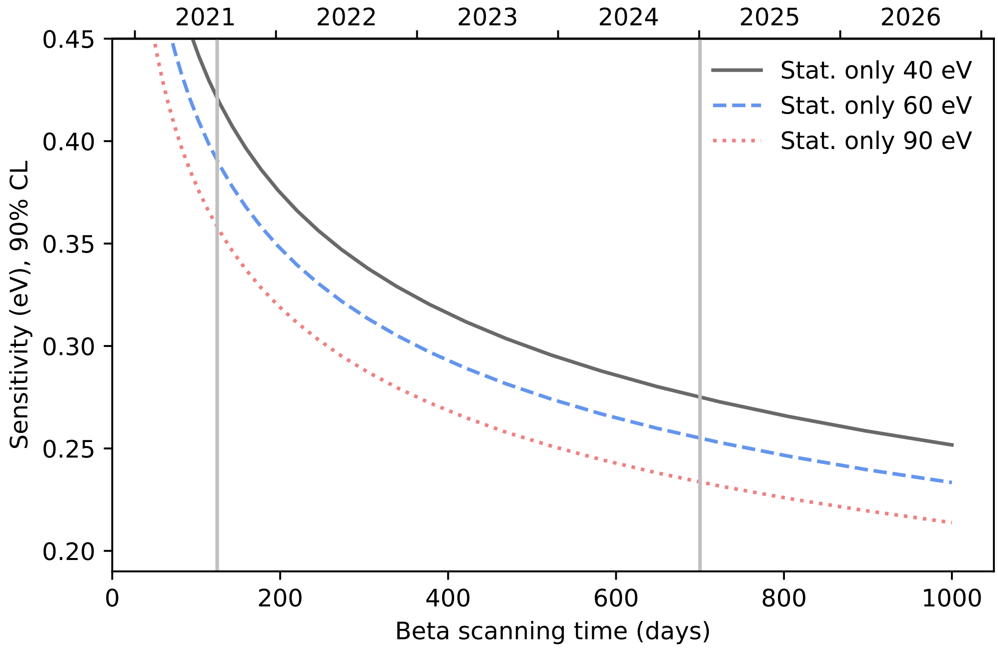

Figure 5.12: Sensitivity projection (statistics only) assuming parameters of the fifth KATRIN campaign for 40 eV (black solid line), 60 eV (blue dashed line) and 90 eV (red dotted line) fit range. At the end of 2024, assuming the here investigated scenario, 700 full days of statistics could be collected. The final 1000 days of statistics could be gained under the assumed conditions in late 2026. August 2021 and end of 2024 are marked with a grey line.

As explained before, the starting sensitivity in the here studied scenario is the assumed to realistically be reached sensitivity of 0.42 eV in the 40 eV fit range after 125 days. For the 60 eV fit range this improves to 0.39 eV and for the 90 eV fit range to 0.36 eV respectively. After 700 days (at the end of 2024) 0.28 eV can be reached in the 40 eV fit range. In the 60 eV fit range 0.26 eV can be reached and in the 90 eV fit range 0.23 eV. After 1000 days (late 2026) this improves to a statistics only sensitivity of 0.25 eV in the 40 eV fit range, 0.23 eV in the 60 eV fit range and 0.21 eV in the 90 eV fit range.

If one now accounts for all systematic uncertainties as summarized in table 5.3, the sensitivity gain due to an extended fit range drastically decreases. For a low amount of collected statistics ($\mathcal{O}$(100 days)) the sensitivity improvement by extending the fit range from 40 eV to 60 eV is about 0.014 eV. A further extension to 90 eV only yields an improvement of another 0.001 eV. For a large amount of statistics ($\mathcal{O}$(1000 days)) the gain is only on the order of $\mathcal{O}$(0.1 meV) (40 eV to 60 eV) and yet another 0.003 eV (60 eV to 90 eV). The corresponding sensitivity curves are shown in figure 5.13a.

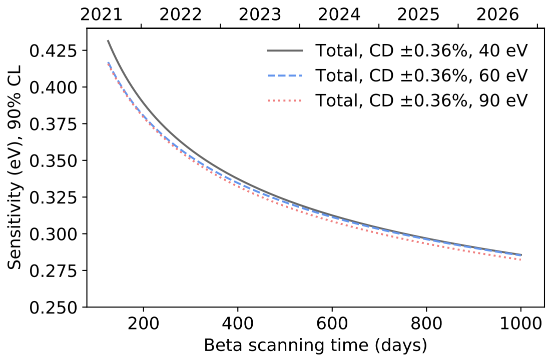

(a) Sensitivity curves total with ±0.36% column density uncertainty.

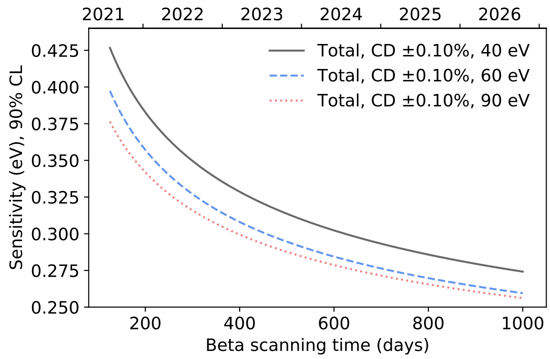

(b) Sensitivity curves total with ±0.10% column density uncertainty.

Figure 5.13: Sensitivity curves for 40 eV (black solid line), 60 eV (blue dashed line) and 90 eV fit range (red dotted line). For the case of ±0.36% column density uncertainty (a) the sensitivity gain by a fit range extension is only on the order of $\mathcal{O}$(meV). For an improved column density uncertainty of ±0.10% (b) the effect is notably higher. Especially the extension from 40 eV to 60 eV yields an improvement of about 0.03 eV (low statistics) and about 0.02 eV (high statistics).

This described marginal sensitivity improvement is dominated by the uncertainty on the column density. If one now assumes an improved column density uncertainty of ±0.10% instead of the before considered ±0.36%, the sensitivity gain by an extended fit range is notably higher. For low statistics ($\mathcal{O}$(100 days)) the sensitivity improves about 0.03 eV by an extension from 40 eV to 60 eV and about another 0.02 eV by a further extension to 90 eV. For high statistics ($\mathcal{O}$(700-1000 days)) about 0.015 eV are gained (40 eV to 60 eV) and still another few meV for a further extension to 90 eV. The sensitivity curves considering the the improved column density uncertainty are shown in figure 5.13b. The individual sensitivity results are summarized in table 5.10 for all considered fit ranges and column density uncertainties as well as for the statistics only case.

Fit range	**2021 (125 d)**	**2024 (700 d)**	**2026 (1000 d)**
Statistics only:			
40 eV	0.4210 eV	0.2750 eV	0.2517 eV
60 eV	0.3905 eV	0.2550 eV	0.2334 eV
90 eV	0.3581 eV	0.2336 eV	0.2138 eV
Total and CD uncertainty ±0.36%:			
40 eV	0.4313 eV	0.3039 eV	0.2856 eV
60 eV	0.4170 eV	0.3031 eV	0.2852 eV
90 eV	0.4158 eV	0.3001 eV	0.2823 eV
Total and CD uncertainty ±0.10%:			
40 eV	0.4266 eV	0.2932 eV	0.2742 eV
60 eV	0.3973 eV	0.2763 eV	0.2595 eV
90 eV	0.3765 eV	0.2714 eV	0.2562 eV

Table 5.10: Sensitivity for different fit ranges after 125 days of statistics (August 2021), after 700 days (end 2024) and after 1000 days (late 2026). Top: Statistics only, middle: Total and CD uncertainty ±0.36%, bottom: Total and CD uncertainty ±0.10%. For better comparison the sensitivities are indicated with an accuracy up to 0.1 meV.

To get a better understanding of the impact of the individual systematics, a systematics breakdown for 700 days of statistics was done similar to the one in figure 5.6. This time however, the most dominant systematics are investigated for each fit range individually to also see how the uncertainty changes when also data further away from the endpoint is considered.

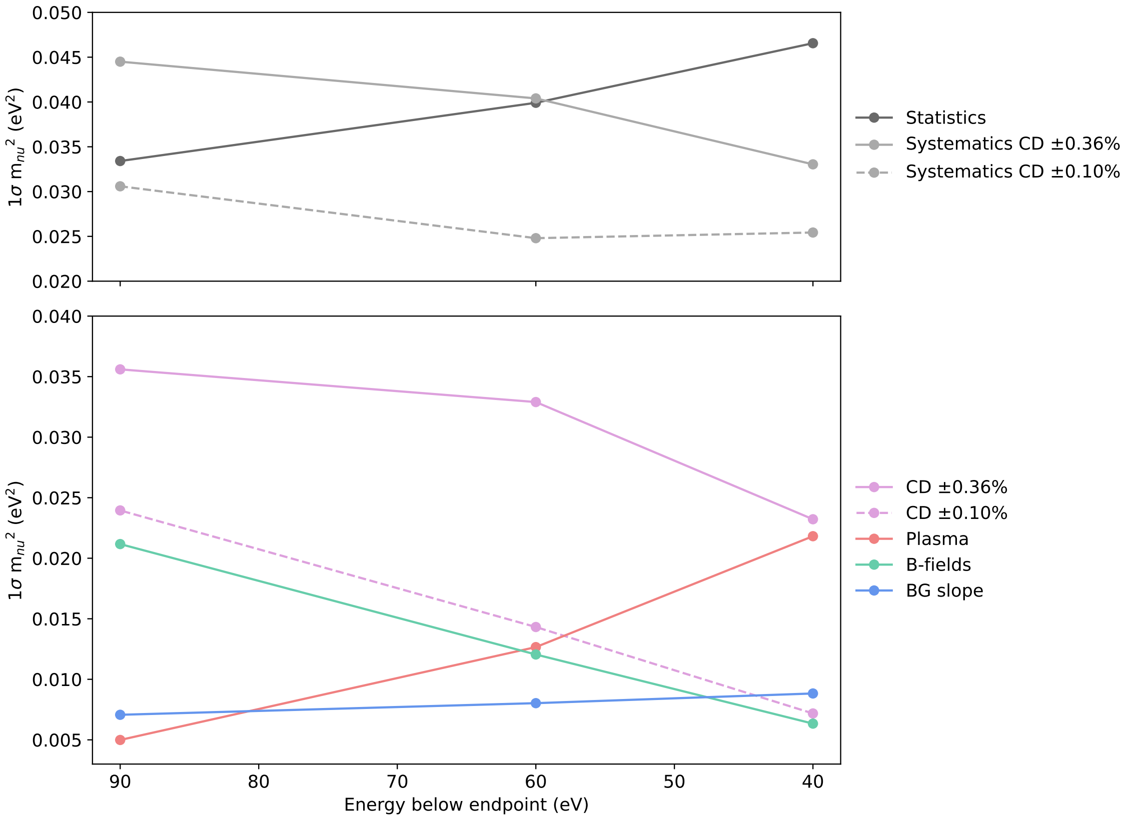

Figure 5.14: Individual systematics for different fit ranges for 700 days of statistics. Top: For a column density uncertainty of $\pm 0.36\%$ KATRIN is statistics dominated in the 40 eV fit range, systematics and statistics balanced in the 60 eV fit range and systematics dominated in the 90 eV fit range. For an improved column density uncertainty of $\pm 0.10\%$ KATRIN remains statistics dominated and the overall error decreases significantly. Bottom: Individual impact of the most dominant systematic effects according to table 5.3 and in addition for the case of an improved uncertainty on the column density from $\pm 0.36\%$ to $\pm 0.10\%$.

The breakdown is shown in figure 5.14. On the top the behaviour of the statistics only error (black) and the error arising from all systematic effects combined (grey) are shown. In the case of an uncertainty of $\pm 0.36\%$ on the column density, KATRIN is statistics dominated in the 40 eV fit range and systematics dominated in the 90 eV fit range. In the 60 eV fit range the systematic and statistical uncertainty are balanced. For an improved column density uncertainty of $\pm 0.10\%$ the systematic uncertainty would decrease significantly. KATRIN could therefore yield better sensitivities and would still be statistics dominated in all fit ranges.

The bottom graph shows now the behaviour of the most dominant systematic effects depending on the fit range. If a column density uncertainty of $\pm 0.36\%$ is considered, it is the most dominant effect already in the 40 eV fit range. It is followed by the uncertainty on the source electric potential (here again called plasma). Both show an uncertainty of about $0.02\,\mathrm{eV}^2$. The column density is however harder to determine if one evaluates the spectrum further away from the endpoint as more scattering related effects occur. Therefore also the error related to the column density increases for an increased fit range. As introduced in chapter 3.3, the effect related to the source plasma manifests itself as a shape distortion of the spectrum. This is easier to determine when also data collected further away from the endpoint in considered and therefore the plasma related error decreases for an increased fit range. If an improved column density uncertainty of $\pm 0.10\%$ is considered, the plasma uncertainty dominates in the 40 eV fit range, as the error connected to the column density decreases to less than $0.01\,\mathrm{eV}^2$. In the 60 eV fit range the plasma and column density related error are somewhat balanced both between $0.01\,\mathrm{eV}^2$ and $0.02\,\mathrm{eV}^2$. In the 90 eV fit range the column density related uncertainty is then again the dominant effect.

The error related to the source and maximum magnetic fields, here indicated as B-fields, is in the 40 eV fit range with $0.006\,\mathrm{eV}^2$ relatively low. As the magnetic field uncertainty is however as well sensitive to scattering effects, the error increases with an increased fit range. The error related to the background slope is comparably low (less than $0.01\,\mathrm{eV}^2$) and slightly decreases for an extended fit range, as the background is for higher rates easier to distinguish from signal.

5.4.2 Increased acceptance angle

In chapter 3.1.4 the acceptance angle of the KATRIN experiment was introduced as

$$\Theta_{\mathrm{max}} = \arcsin\left(\sqrt{\frac{B_{\mathrm{source}}}{B_{\mathrm{max}}}}\right) \tag{5.5}$$

in adiabatic approximation. In the formerly used KATRIN setting the magnetic fields are $B_{\mathrm{source}} = 2.51\,\mathrm{T}$ and $B_{\mathrm{max}} = 4.24\,\mathrm{T}$. Hence, the maximum acceptance angle was $\Theta_{\mathrm{max}} = 50.3°$. Another way besides increasing the fit range is to change the magnetic field settings in a way that the maximum acceptance angle increases. This idea was applied to simulations to investigate the sensitivity improvement it would yield. The idea has first been discussed in early 2020 and has been further investigated by Ferenc Glück and colleagues in 2022 [36].

For the here investigated scenario the acceptance angle enhancement is achieved by applying a scale factor to all magnetic field strengths after the WGTS. Not only the maximum magnetic filed is changed because the magnetic fields in the DPS and the CPS should stay lower than the pinch magnetic field (here referred to as the maximum magnetic field) even within some safety margins. The magnetic flux and hence the magnetic flux tube that is present at the FPD are however also reduced by the scale factor, which translates into a reduction of the statistics gain. The flux tube reduction is taken into account in the data simulation with `Fitrium` by also scaling the magnetic field at the detector. The here applied scale factor is 2/3 as supposed in [36].

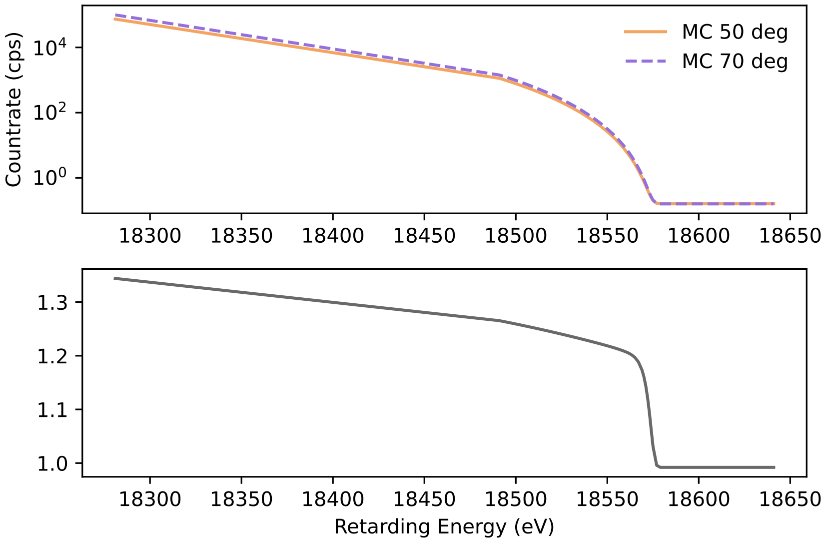

Figure 5.15: Rate with increased acceptance angle. Top: Rate considering $\Theta_{\mathrm{max}} = 70.4°$ (purple dashed line) versus $\Theta_{\mathrm{max}} = 50.3°$ (orange solid line). Bottom: fraction of count rate with increased acceptance angle over regular acceptance angle. In the here considered 40 eV fit range the enhancement is up to about 24%.

All parameters are therefore as in table 5.3 and 5.4 except the magnetic fields which are set to $B_{\mathrm{FPD}} = 1.613\,\mathrm{T}$, $B_{\mathrm{transport}} = 2.4\,\mathrm{T}$, $B_{\mathrm{max}} = 2.83\,\mathrm{T}$ and $B_{\mathrm{ana}} = 3.66 \times 10^{-4}\,\mathrm{T}$ while the source magnetic field stays the same with $B_{\mathrm{source}} = 2.51\,\mathrm{T}$. The maximum acceptance angle in this setting is hence $\Theta_{\mathrm{max}} = 70.4°$. Also considering the adapted flux tube at the detector this yields a rate enhancement of up to 24% in the 40 eV fit range and up to 27% further in the spectrum. The difference in count rate for the two considered acceptance angles is shown in figure 5.15. Not further investigated here is the change in scattering probabilities the transmitted electrons show. In general, the electrons in the wider angle setting scatter more often, as their path length increases.

In the following step the sensitivity can be calculated assuming the increased acceptance angle. This is done as described earlier in this chapter. The assumed systematic uncertainties are the ones from table 5.3. The sensitivities gained with both here considered acceptance angles, only depending on the amount of statistics, are shown in figure 5.16.

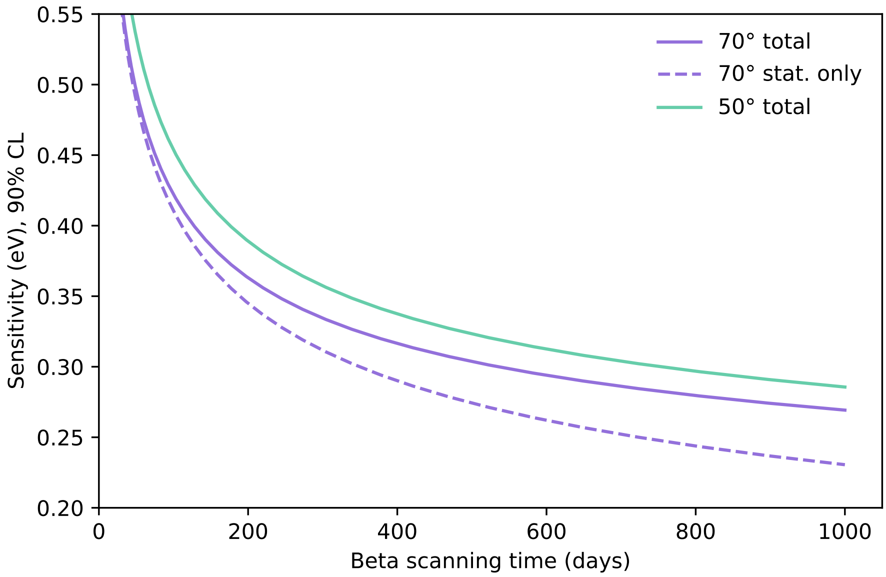

Figure 5.16: Sensitivity with increased acceptance angle depending on the amount of β-scanning days. Purple solid line: Sensitivity with increased acceptance angle (70.4°) considering all systematic effects. Purple dashed line: Increased acceptance angle statistics only. Green line: Comparison to the 2021 projection considering the same systematics and the nominal acceptance angle of 50.3°.

The here presented comparison shows the sensitivity improvement that would have been made if KATRIN had used the increased acceptance angle setting from the beginning. The sensitivity improvement after 125 days of statistics is 0.030 eV. After 700 days it is 0.018 eV and after the full 1000 days 0.016 eV.

In figure 5.17 two scenarios are considered in which the increased acceptance angle setting is introduced after a certain time of measuring in the nominal setting. Figure 5.17a shows what sensitivity could have been reached if the increased acceptance angle setting had been applied before the sixth KATRIN campaign in August 2021. At the end of 2024 a sensitivity improvement of 0.015 eV could have been made and after 1000 days of statistics the improvement would have been 0.014 eV. Figure 5.17b shows the sensitivity improvement that could still be made if after the regular KATRIN data taking period until the end of 2024, starting from January 2025 the measurements are continued until late 2026 with the increased acceptance angle. In this way after the full 1000 days of statistics a sensitivity improvement of 0.007 eV could be made. At this point it has to be taken into account that before the setting with the increased acceptance angle could be put into beta scanning operation, further systematics measurements would have to be performed to better understand the plasma and column density dependence in that setting. This could add another delay if exceeding the time considered for calibration measurements etcetera in the efficiency estimation. It is also possible that for example the plasma uncertainty increases for the larger acceptance angle which could further reduce the sensitivity improvement.

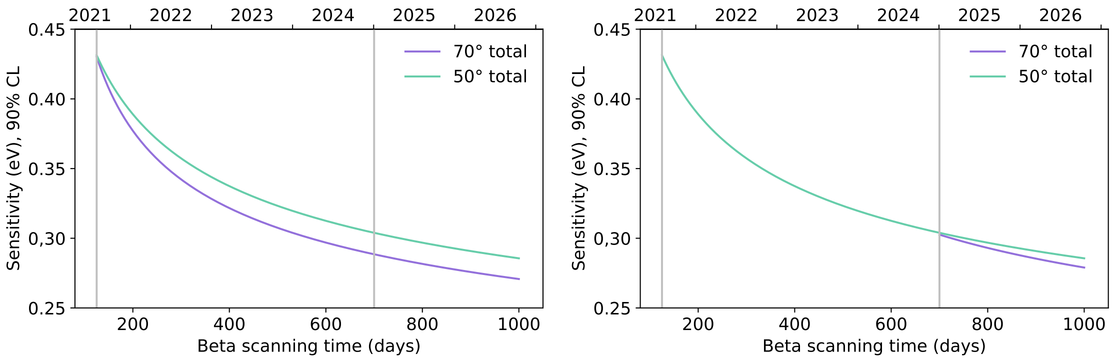

(a) Sensitivity improvement if the increased acceptance angle setting would have been applied before the sixth KATRIN campaign in August 2021.

(b) Sensitivity improvement if the increased acceptance angle setting is applied at the end of 2024 and measurements are taken until late 2026.

Figure 5.17: Sensitivity with increased acceptance angle (70.4°, purple line) from August 2021 (a) and January 2025 (b) after and compared to measuring with the nominal acceptance angle (50.3°, green line).

5.5 Background reducing scenarios

In chapter 5.4 two ways to enhance the signal in KATRIN have been investigated. Another way to improve the signal over background ratio $\frac{\mathcal{S}}{\mathcal{B}}$ is to reduce the background rate that arrives at the detector. In 5.5.1 the sensitivity that could have been reached with the background rate predicted in the technical design report (TDR) from 2004 is calculated. In 5.5.2 the effect of a novel active transversal energy filter (aTEF) is investigated.

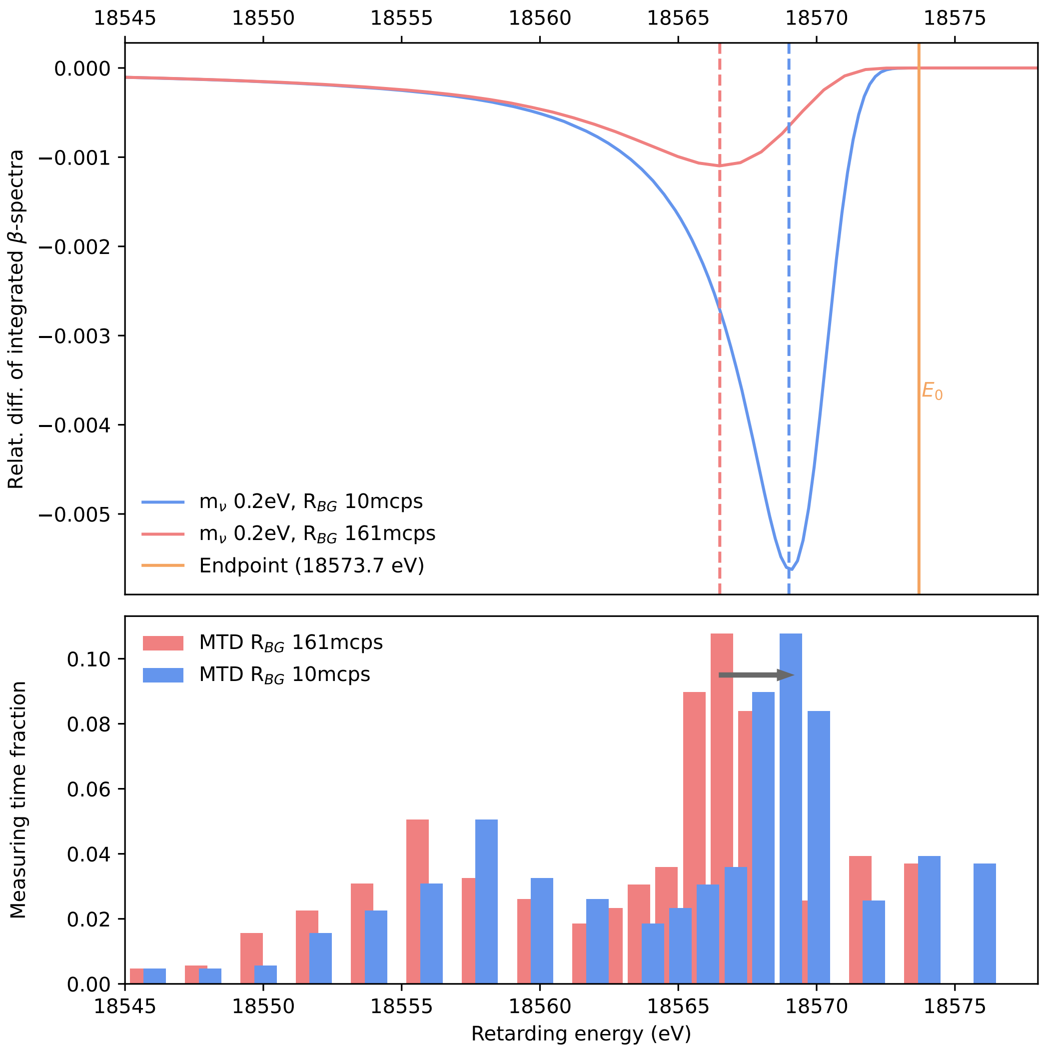

Figure 5.18: Measurement Time Distribution (MTD) adaptation for design background rate. Top: Relative difference of integrated β-spectra considering the imprint of a neutrino mass of 0.2 eV for the current background (red line) and the TDR background (blue line). Bottom: MTD used for the current measurements (red) and optimized MTD for the TDR background rate of 10 mcps (blue).

5.5.1 Design background rate

In the technical design report (TDR) from 2004 a background rate of 10 mcps distributed over 148 pixels was predicted [29]. Due to several effects this design background rate could not be achieved in the operating KATRIN system. The first source of background that could however be eliminated, was the pre-spectrometer (cf. chapter 3.1.4). By shutting it off, the penning background is avoided. As explained in 5.3.2, a further background reduction could be made by applying the SAP setting. Therefore, the current background rate in KATRIN is 136 mcps over 126 active pixels. Considering the amount of active pixels, the TDR background rate scales down to 8.5 mcps.

MTD adaptation

The Measurement Time Distribution (MTD) is optimized for the actual KATRIN setting, considering also the prevailing background rate. For different background rates, the signal of a neutrino mass is most present at different retarding energies. This can be visualized by comparing the integrated β-spectrum assuming a non-vanishing neutrino mass (here 0.2 eV are considered) to the spectrum without any neutrino mass imprint for the background rates of interest [37].

To obtain an optimized MTD for the data simulation considering the TDR background rate, the current MTD is shifted by the difference between the neutrino mass imprint peaks for the different background rates. This procedure is visualized in figure 5.18. Here the background rates at the FPD are considered, regardless of the amount of active pixels. The actual considered background rates in the analysis are yielded by scaling by the amount of active pixels. As the peak signal of a non-zero neutrino mass is shifted by 2.5 eV for the current background rate and the design background rate, also the MTD is shifted by 2.5 eV for the data simulation of the TDR scenario. It has to be noted that some benefits of the before optimized MTD are lost in that way, as for example some systematics properties etcetera.

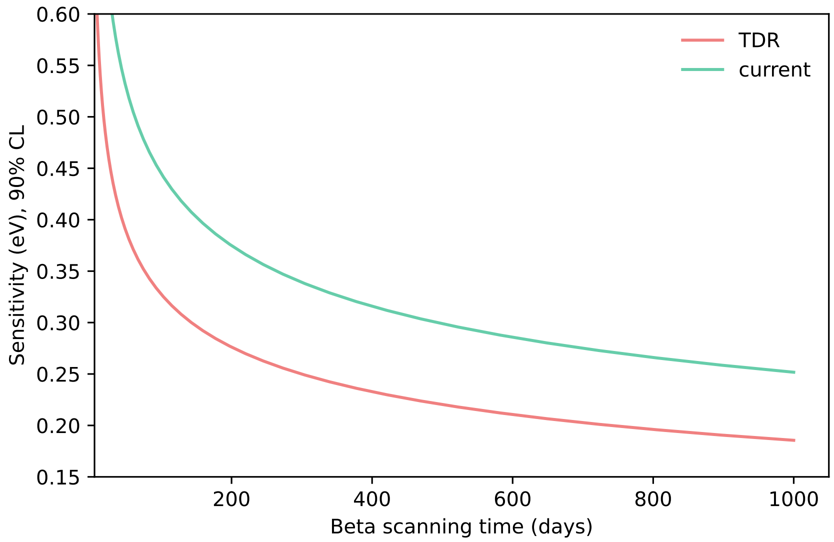

Figure 5.19: Sensitivity (statistics only) with the TDR background rate (red line) and the current background rate (green line).

Statistics only

To investigate the sensitivity that would have been reachable with the background rate predicted in the TDR a MC data sample has been generated considering all parameters like in table 5.3 and 5.4. The sensitivity considering the statistical uncertainty only depending on the amount of collected statistics is shown in figure 5.19 compared to the sensitivity reached with the 2021 projection.

Background	125 d	700 d	1000 d
8 mcps	0.31 eV	0.20 eV	0.19 eV
136 mcps	0.42 eV	0.27 eV	0.25 eV

Table 5.11: Sensitivity (statistics only) with the TDR background rate and the current background rate.

The sensitivities that could have been reached with the TDR background rate compared to the ones considering the current background rate of 136 mcps are summarized in table 5.11. The statistics only one sigma uncertainty on m_ν^2 of $0.017\,\mathrm{eV}^2$ was predicted to be achieved after 1000 days of statistics. In the here presented scenario after 1000 full days of statistics (realistically reachable in late 2026) the statistics only one sigma uncertainty on m_ν^2 is only $0.021\,\mathrm{eV}^2$ as not all parameters could been set as designed. This is mainly due to the column density which can only be hold at 75% in the current measurements and due to the reduced amount of active pixels (126 of 148). Considering that, $0.017\,\mathrm{eV}^2$ could only be reached after additional 550 days of statistics.

Sensitivity scenarios with TDR background

In the next step, possible sensitivity improvements that could have been or could still be made in the future, are investigated. To estimate the sensitivity considering the total uncertainty, the desired $0.017\,\mathrm{eV}^2$ systematic uncertainty is added quadratically to the statistical uncertainty. In figure 5.20 two scenarios are investigated.

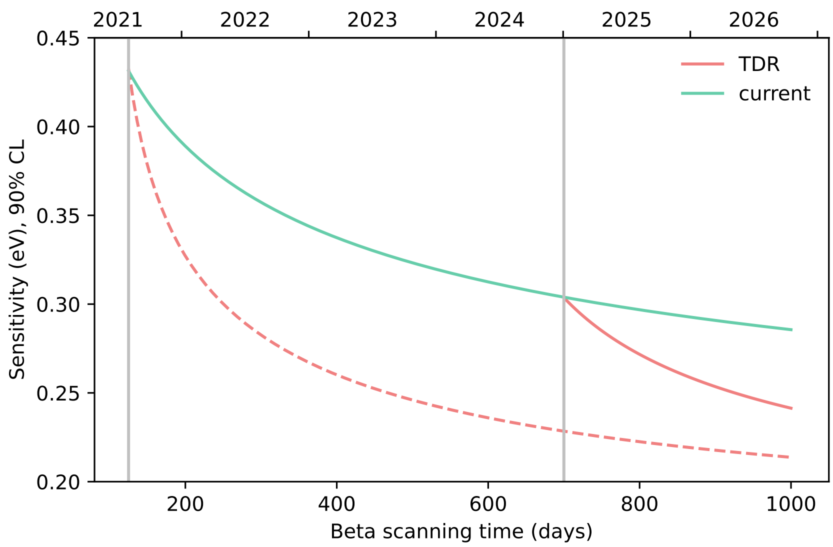

Figure 5.20: Sensitivity scenarios with TDR background: The green line visualizes the sensitivity prospects of the 2021 projection. The red dashed line shows the sensitivity that could have been reached, if before the sixth measurement campaign in August 2021 the TDR background rate had been realized. The solid red line shows the sensitivity that could be reached if the TDR background rate was realized for additional measurements starting in January 2025.

If the TDR background rate and the TDR systematic uncertainty were realized already in 2021, by the end of 2024 a sensitivity of 0.23 eV could have been achieved. If one could realize the TDR background and systematics for additional measurements starting in 2025 a sensitivity of 0.24 eV can be reached in late 2026. To finally reach the goal sensitivity of 0.2 eV the measurements would have to be continued until 2000 days of statistics are collected which could only be the case after another ~ 6 years considering the overall assumed data taking efficiency.

In general it has to be noted that for the here presented sensitivity scenarios two simulated data sets are investigated together (2021 projection and TDR scenario). For the estimations in figure 5.20 the TDR sensitivity curve has simply been shifted to the crossing sensitivities of 0.43 eV in August 2021 and 0.30 eV at the end of 2024. This is assumed to be in good approximation of the theoretically required combined fit to give sensitivity prospects. However, this assumption has still to be verified in the future.

5.5.2 Background reduction with an active transversal energy filter

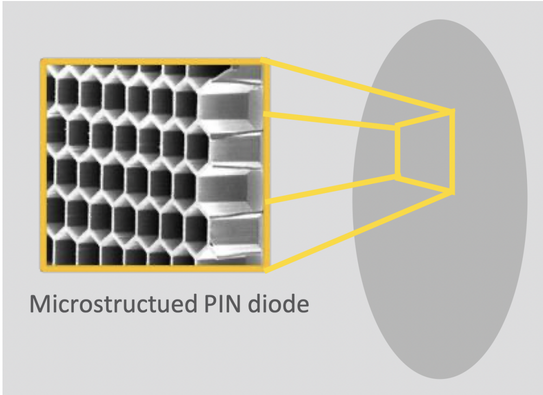

Figure 5.21: Schematic view of an aTEF on the modified FPD. Figure taken from [38].

The active transversal energy filter (aTEF) was first discussed in 2020 and is currently in production and under further investigation. The concept makes use of the fact that the background electrons arriving at the detector have a significantly lower polar angle than the signal electrons. An aTEF has a comb like structure as shown in figure 5.21. As the background electrons have a lower polar angle, they pass the structure unnoticed while the signal electrons with a higher polar angle hit the walls of the combs where they are detected. The aTEF is therefore a detector and a background filter at the same time. There are two types of aTEFs under investigation. One uses a silicon semiconductor detector (si-aTEF) and the other a scintillator combined with a photodetector (scint-aTEF) [39]. Figure 5.21 shows a si-aTEF. The implementation of an aTEF is assumed to reduce the background rate by a factor of three. A corresponding MC data set has been simulated considering the same MTD as for the TDR scenario. However, also the data taking efficiency reduces by a certain factor, as besides the filtered out background electrons also some signal electrons can pass the aTEF without being detected. The additional efficiency correction is here assumed to be 80%.

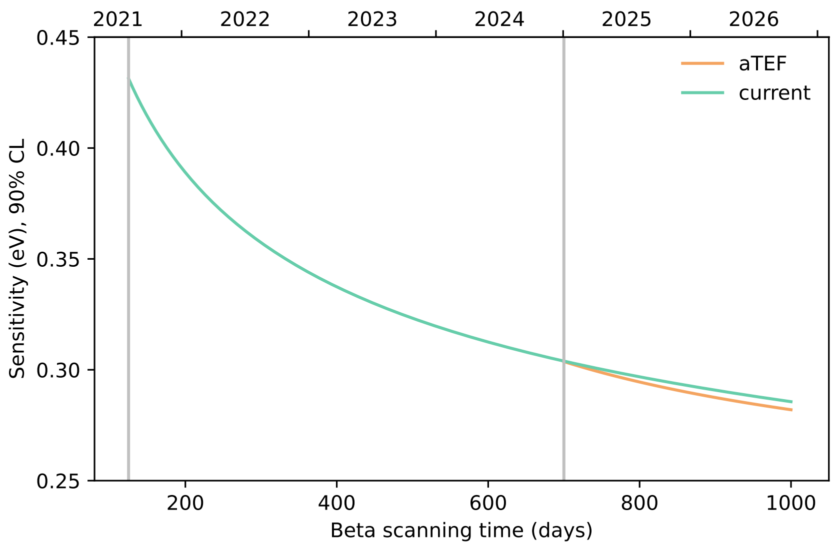

Figure 5.22: Sensitivity that could be reached with an active transversal energy filter implemented from 2025 (orange line) compared to the 2021 projection (green line).

To estimate the total sensitivity of this scenario, the statistics only sensitivity was calculated with the aTEF MC sample and the regular parameters from table 5.3 and 5.4. As a systematic uncertainty $0.033\,\mathrm{eV}^2$ are assumed as yielded for the 2021 projection after 700 days of statistics (cf. figure 5.6). The sensitivity improvement with an aTEF, implemented from 2025 is shown in figure 5.22. The sensitivity that could be reached is 0.28 eV in late

2026. This would bring an improvement of 0.01 eV compared to the 2021 projection. Note that here no further delay due to implementation or additional unaccounted systematic effects are taken into consideration.

5.6 Conclusive sensitivity prospect

In a last step, all considerations that have been made throughout this thesis are put together to give a conclusive sensitivity prospect. The currently published result from 2022 is $m_{\nu_e} < 0.80\,\text{eV}(90\ \%\ \text{C.L.})$. With the data taken until 2021, a publication is planned for soon this year which is assumed to be able to constrain the neutrino mass to $m_{\nu_e} < 0.43\,\text{eV}(90\ \%\ \text{C.L.})$. The parameters and systematic uncertainty for the measurements taken until the end of 2022 are for the most part known and will probably allow a sensitivity of 0.385 eV. It is then assumed that from 2023 on, the systematics are understood better (especially the column density). Therefore the systematic uncertainty is assumed to be improved from conservatively considered $0.065\,\text{eV}^2$ until the end of 2022 to $0.025\,\text{eV}^2$ from 2023. To also increase the amount of collected statistics it is currently discussed to continue the measurements until the end of 2025. Without considering the β-scanning efficiency this equals 1000 measurement days.

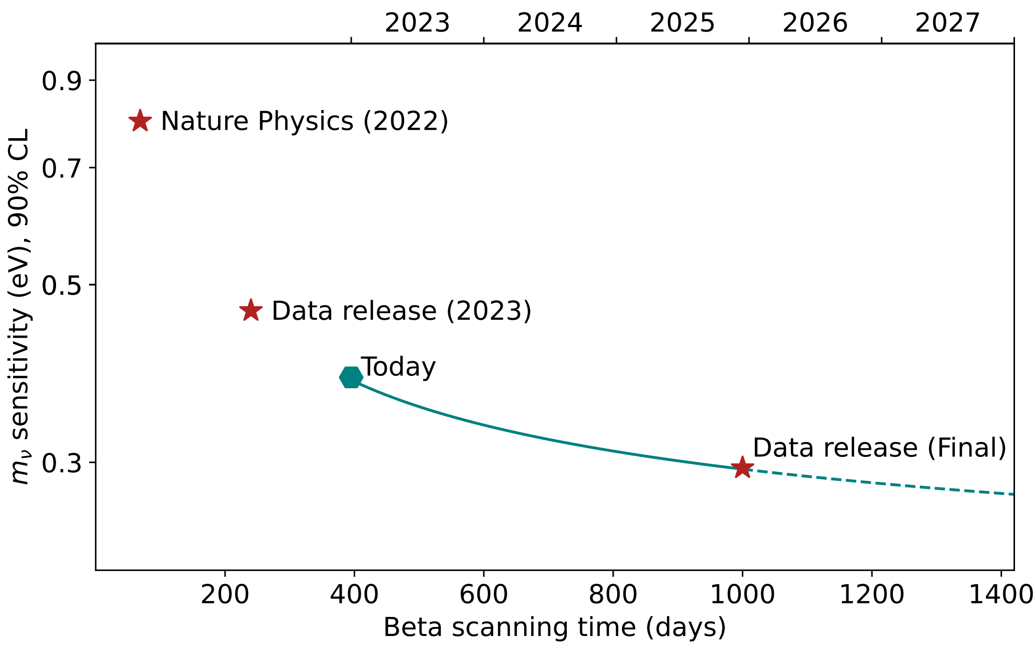

Figure 5.23: Conclusive sensitivity prospect. Previous and planned publications are marked with a red star. From 2023 on, the measurements are assumed to be taken with an overall systematic uncertainty of $0.025\,\text{eV}^2$. The corresponding sensitivity is indicated by the green line. The hexagon indicating *today* marks January 1, 2023.

Taking all the above mentioned considerations into account a conclusive sensitivity prospect can be made for the KATRIN experiment reachable by the end of 2025:

$$m_{\nu_{\text{e, KATRIN 1000 days}}} < 0.295\,\text{eV}(90\ \%\ \text{C.L.}). \tag{5.6}$$

All mentioned dates and results are visualized in figure 5.23. Note that here the actual amount of 205 β-scanning days that were performed until August 2021, are considered, instead of the 125 days that would have yielded the same sensitivity under the current conditions.

5.7 Conclusive discovery potential prospect

The results presented in 5.6 leave still room for a potential discovery. The corresponding discovery potentials are calculated according to equation 4.20 and considering all information from 5.6. The final D.P. prospects are 0.40 eV for the 3σ D.P. and 0.51 eV for the 5σ D.P. by the end of 2025, which would correspond to 1000 measurement days (not considering the β-scanning efficiency). The discovery potentials are visualized in figure 5.24.

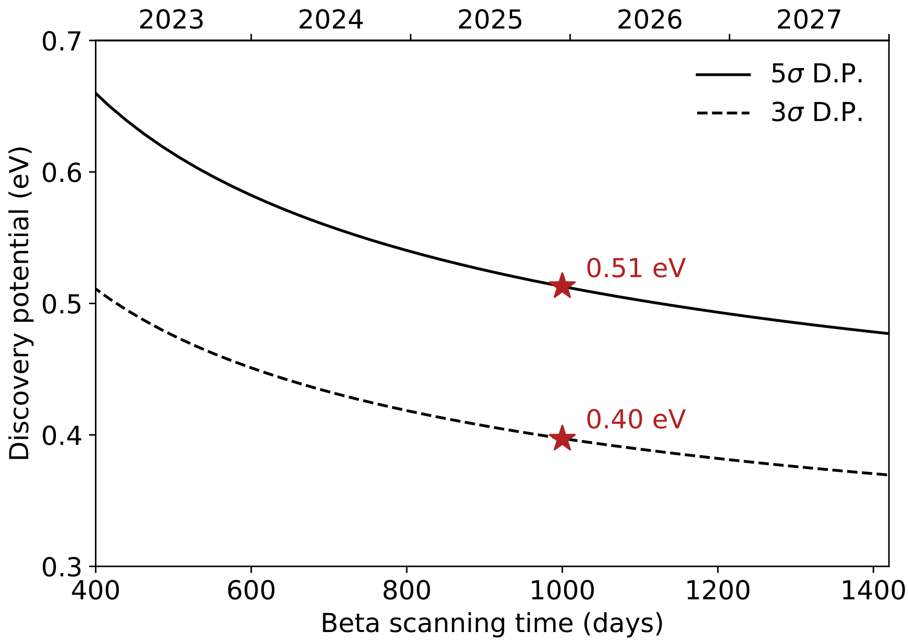

Figure 5.24: Conclusive discovery potential prospect. By the end of 2025 (1000 days) the 3σ D.P. is 0.40 eV and the 5σ D.P. is 0.51 eV (red stars).

Chapter 6

Conclusion

The goal of the KATRIN experiment is to reach a sensitivity of $m_{\nu_e} < 0.2\,\mathrm{eV}$ (90 % C.L.) after 1000 β-scanning days. The objective of this thesis was to investigate the feasibility and potential improvements concerning this target. From the performed studies it can be concluded that in the setting from 2021, until the end of 2024, data can be collected that equals 700 β-scanning days. This yields a statistical sensitivity of 0.27 eV. Considering all systematic effects with their nominal uncertainty, the sensitivity is 0.30 eV. After 2021, certain complications arose regarding the determination of the uncertainty of the gas density in the tritium source. Therefore the prospect deteriorated. From 2023 on however, the measurements can be continued with better systematics accuracy, as the gas density investigations were successful. Further it is assumed that the measurements with the KATRIN experiment are continued until the end of 2025. Given a total of 1000 measurement days, a total sensitivity of

$$m_{\nu_{\mathrm{e,\ KATRIN\ 1000\ days}}} < 0.295\,\mathrm{eV}(90\ \%\ \mathrm{C.L.})$$

can be reached, including all systematic effects. This corresponds to a 3σ discovery potential of 0.40 eV and 0.51 eV at 5σ. The studies performed in this thesis, leading to this result, are summarized in the following.

Averaged multi-patch approach As the full neutrino mass analysis method is highly complex and thus time consuming, a simplified method has been applied. Instead of following the regular approach, the analysis of the investigated scenarios has been performed, assuming a setting corresponding to the average performance of the fourteen detector patches. The impact on the obtained sensitivities is on the order of 1 meV and thus negligible for the forecasts. In this way, a fast and resistant method is provided also for future estimations and cross-checks.

Sensitivity improvement by a shifted analyzing plane After a few years of operation time, the KATRIN spectrometer setting has been changed in a way that could reduce the background by approximately a factor of two. This has been realized by reducing the space between the analyzing plane and the detector. Without this background improvement a sensitivity of 0.36 eV would have been obtained at the end of 2024, approximately 0.06 eV worse than with the actually achieved performance.

Signal enhancement The sensitivity of the KATRIN experiment is currently limited by the statistical uncertainty. Therefore two signal enhancing scenarios have been investigated. By expanding the currently considered fit range of starting at 40 eV below the endpoint to 60 eV or even 90 eV, additional signal electrons that carry neutrino mass information are included in the fit. For the currently assumed gas density uncertainty of $\pm$ 0.36% this would not yield a sensitivity improvement, as the impact of the gas density uncertainty increases deeper in the spectrum. However, under the consideration of a well understood gas density in the source ($\pm$ 0.1%), the sensitivity would improve by about 0.015 eV for a fit range extension from 40 eV to 60 eV. Considering the 60 eV fit range and a gas density uncertainty of $\pm$ 0.1%, the statistical and systematic uncertainty of the KATRIN experiment would be balanced at the end of 2024.

The second investigated way to enhance the signal is an increased acceptance angle. In the current KATRIN setting electrons with a maximum starting angle of 50.3° can reach the detector. By adapting the magnetic field configurations, the acceptance angle could be increased to 70.4°. This would yield a statistics enhancement of up to 24% in the 40 eV fit range, also due to a higher amount of scattered electrons. Applying the increased acceptance angle from 2025, a sensitivity improvement of 0.01 eV can be made in late 2026, if the measurements are continued.

Background reduction The background in the KATRIN experiment was originally assumed to be about one order of magnitude lower than it currently is. If the design background rate had been realized from the beginning, the statistical sensitivity at the end of 2024 would be 0.07 eV better than in the current setting. Given a lower column density in the current KATRIN setting and some inactive pixels, this number still deviates from the designed statistical sensitivity. If the measurements are continued from 2025 with the designed background rate and a combined systematic uncertainty of 0.017 eV^2, a sensitivity of 0.24 eV can be reached in late 2026. By implementing an active transversal energy filter (aTEF) from 2025, the sensitivity can be improved by 0.01 eV in late 2026, compared to the current setting.

List of Acronyms

$0\nu\beta\beta$ neutrinoless double β-decay.

$2\nu\beta\beta$ neutrino accompanied double β-decay.

aTEF active transversal energy filter.

BED Binary Encounter Dipole.

C.L. Confidence Level.

CMB Cosmic Microwave Background.

CPS Cryogenic Pumping System.

D.P. discovery potential.

DAQ data acquisition.

DPS Differential Pumping System.

e-gun electron gun.

FPD Focal Plane Detector.

FSD Final State Distribution.

KATRIN KArlsruhe TRItium Neutrino.

KIT Karlsruhe Institute of Technology.

KNM KATRIN neutrino mass.

LLH likelihood.

MAC-E Magnetic Adiabatic Collimation with Electrostatic.

MC Monte Carlo.

MTD Measurement Time Distribution.

NAP normal analyzing plane.

NN neural net.

PMF probability mass function.

ROI region of interest.

RW rear wall.

SAP shifted analyzing plane.

TDR technical design report.

TLK Tritium Laboratory Karlsruhe.

WGTS Windowless Gaseous Tritium Source.

List of Figures

List of Tables

Bibliography

[1] Wolfgang Pauli. Pauli letter collection: letter to Lise Meitner. Typed copy, http://cds.cern.ch/record/83282, 1930.

[2] E. Fermi. An attempt of a theory of beta radiation. 1. *Z. Phys.*, 88:161–177, 1934.

[3] David Griffiths. *Introduction to Elementary Particles.* 2004 WILEY-VCH Verlag GmbH & Co. KGaA, 1987. ISBN 9780471603863, DOI 10.1002/9783527618460.

[4] C. L. Cowan, F. Reines, F. B. Harrison, H. W. Kruse, and A. D. McGuire. Detection of the free neutrino: a confirmation. *Science*, 124(3212):103–104, 1956.

[5] Bogdan Povh. *Teilchen und Kerne: eine Einführung in die physikalischen Konzepte, 9. Auflage.* Springer Spektrum, 2014. ISBN 9783642378218, DOI 10.1007/978-3-642-37822-5.

[6] Q. R. Ahmad et al. Direct evidence for neutrino flavor transformation from neutral-current interactions in the sudbury neutrino observatory. *Physical Review Letters*, 89(1), jun 2002. https://doi.org/10.1103%2Fphysrevlett.89.011301.

[7] Christopher W. Walter. Experimental neutrino physics, 2008. https://arxiv.org/abs/0810.3937.

[8] Y. Fukuda et al. Evidence for oscillation of atmospheric neutrinos. *Physical Review Letters*, 81(8):1562–1567, aug 1998. https://doi.org/10.1103%2Fphysrevlett.81.1562.

[9] Jose Bernabeu, Julien Lesgourgues, and Sergio Pastor. Neutrino mass from cosmology. *Advances in High Energy Physics*, 2012:608515, 2012. https://doi.org/10.1155/2012/608515.

[10] N. Aghanim et al. Planck 2018 results. *Astronomy and Astrophysics*, 641:A6, sep 2020. https://doi.org/10.1051%2F0004-6361%2F201833910.

[11] M. Agostini et al. Final results of gerda on the search for neutrinoless double-beta-decay. *Physical Review Letters*, 125(25), dec 2020. https://doi.org/10.1103%2Fphysrevlett.125.252502.

[12] Arthur B. McDonald, Andrea Giuliani, and Alfredo Poves. Neutrinoless double-beta decay. *Advances in High Energy Physics*, 2012:857016, 2012. https://doi.org/10.1155/2012/857016.

[13] M. Kleesiek, J. Behrens, G. Drexlin, K. Eitel, M. Erhard, J. A. Formaggio, F. Glück, S. Groh, M. Hötzel, S. Mertens, A. W. P. Poon, C. Weinheimer, and K. Valerius. Beta-decay spectrum, response function and statistical model for neutrino mass measurements with the katrin experiment. *The European Physical Journal C*, 79(3), 2019. https://doi.org/10.1140%2Fepjc%2Fs10052-019-6686-7.

[14] M. et al. Aker. First direct neutrino-mass measurement with sub-ev sensitivity, 2021. https://arxiv.org/abs/2105.08533.

[15] Ch Kraus, B. Bornschein, L. Bornschein, J. Bonn, B. Flatt, A. Kovalik, B. Ostrick, E. W. Otten, J. P. Schall, Th Thümmler, and Ch Weinheimer. Final results from phase II of the mainz neutrino mass searchin tritium beta-decay. *The European Physical Journal C*, 40(4):447–468, apr 2005. https://doi.org/10.1140%2Fepjc%2Fs2005-02139-7.

[16] V. N. Aseev, A. I. Belesev, A. I. Berlev, E. V. Geraskin, A. A. Golubev, N. A. Likhovid, V. M. Lobashev, A. A. Nozik, V. S. Pantuev, V. I. Parfenov, A. K. Skasyrskaya, F. V. Tkachov, and S. V. Zadorozhny. Upper limit on the electron antineutrino mass from the troitsk experiment. *Physical Review D*, 84(11), dec 2011. https://doi.org/10.1103%2Fphysrevd.84.112003.

[17] The KATRIN collaboration and M. Aker et al. The design, construction, and commissioning of the katrin experiment. *Journal of Instrumentation*, 16(08):T08015, aug 2021. https://dx.doi.org/10.1088/1748-0221/16/08/T08015.

[18] Christian Karl. *First Sub-Electronvolt Direct Neutrino Mass Measurement with the KATRIN Experiment.* Dissertation, Technical University of Munich, 2022.

[19] Svante Jonsell, Alejandro Saenz, and Piotr Froelich. Neutrino-mass determination from tritium beta decay: Corrections to and prospects of experimental verification of the final-state spectrum. *Phys. Rev. C*, 60:034601, Jul 1999. https://link.aps.org/doi/10.1103/PhysRevC.60.034601.

[20] M. Aker et al. Precision measurement of the electron energy-loss function in tritium and deuterium gas for the KATRIN experiment. *The European Physical Journal C*, 81(7), jul 2021. https://doi.org/10.1140%2Fepjc%2Fs10052-021-09325-z.

[21] Stefan Groh. *Modeling of the response function and measurement of transmission properties of the KATRIN experiment.* Dissertation, Karlsruhe Institute of Technology, 2015.

[22] M. Aker et al. Analysis methods for the first katrin neutrino-mass measurement. *Physical Review D*, 104(1), 2021. https://doi.org/10.1103%2Fphysrevd.104.012005.

[23] Lisa Schlüter. *Neutrino-Mass Analysis with sub-eV Sensitivity and Search for Light Sterile Neutrinos with the KATRIN Experiment.* Dissertation, Technical University of Munich, 2022.

[24] Christoph Köhler. Determination of the column density for the katrin neutrino mass measurement. International School of Nuclear Physics, 2019.

[25] Matthias Weidenthaler. *Systematic Uncertainties of the KATRIN Neutrino Mass Measurement Associated with Beta Decays on the Rear Wall of the Experiment.* Master's thesis, Technical University of Munich, 2022.

[26] Moritz Benedikt Machatschek. *A Phenomenological Theory of KATRIN Source Potential Systematics and its Application in Krypton-83m Calibration Measurements.* Dissertation, Karlsruher Institut für Technologie (KIT), 2021.

[27] Anna Katharina Schaller. *Characterization and mitigation of the background in KATRIN.* Dissertation, Technical University of Munich, 2020.

[28] F. M. Fränkle, F. Glück, K. Valerius, K. Bokeloh, A. Beglarian, J. Bonn, L. Bornschein, G. Drexlin, F. Habermehl, M. L. Leber, A. Osipowicz, E. W. Otten, M. Steidl, T. Thümmler, C. Weinheimer, J. F. Wilkerson, J. Wolf, and S. V. Zadorozhny. Penning discharge in the katrin pre-spectrometer. *Journal of Instrumentation*, 2014. DOI: 10.1088/1748-0221/9/07/P07028.

[29] KATRIN Collaboration. Katrin design report 2004. Technical report, Forschungszentrum Jülich, 2005. DOI: 10.5445/IR/270060419.

[30] Christoph Wiesinger. Fpd systematics, increased fit range. KATRIN internal, 2022.

[31] Glen Cowan. *Statistical Data Analysis.* Oxford u.a., Clarendon Press, 1998. ISBN 9780198501558.

[32] Christian Karl. *Analysis of First Tritium Data of the KATRIN Experiment.* Master's thesis, Technical University of Munich, 2018.

[33] Christian Karl, Philipp Eller, and Susanne Mertens. Fast and precise model calculation for katrin using a neural network. *The European Physics Journal C*, 2022. DOI: 10.1140/epjc/s10052-022-10384-z.

[34] Christoph Wiesinger, Alessandro Schwemmer, Christian Karl, and Susanne Mertens. Figure skating knm5. KATRIN analysis internal, 2021.

[35] F. Block, C. Köhler, A. Marsteller, R. Salomon, and S. Schneidewind. Katrin column density report for knm1-5. KATRIN analysis report, 2023.

[36] F. Glück, E. Weiss, and J. Behrens. Higher acceptance angle. KATRIN internal, 2022.

[37] Marco Kleesiek. *A Data-Analysis and Sensitivity-Optimization Framework for the KATRIN Experiment.* Dissertation, Karlsruher Institut für Technologie (KIT), 2014.

[38] Kevin Gauda. Si-atef: status. KATRIN CM internal, 2022.

[39] Anton Huber. The tef-session. KATRIN CM internal, 2022.

Acknowledgements

This thesis would not have been possible without the support of many great people. I especially would like to thank

- Susanne Mertens for giving me the possibility to work in the KATRIN collaboration on one of the most interesting questions in physics;
- Alessandro Schwemmer and Christoph Wiesinger for their great supervision and constant support;
- the whole EDM group and especially Matthias Meier, Korbinian Urban, Christoph Köhler, Joana Bilicki, Daniel Siegmann, Frank Edzards and Lisa Schlüter for the great environment;
- Pia Voigt, Xaver Stribl and Florian Henkes for never letting me forget to get some fresh air especially during stressful periods;
- Markus Wurzer and Andreas Duensing for teaching me how not to give up on myself;
- my partner, friends and family for their thorough understanding and support;
- the German health care system.